Science
AAAS

Supplementary Materials for

A noncoding single-nucleotide polymorphism at 8q24 drives *IDH1*-mutant glioma formation

Connor Yanchus *et al*.

Corresponding authors: Robert B. Jenkins, rjenkins@mayo.edu; Daniel Schramek, schramek@lunenfeld.ca

Science **378**, 68 (2022)
DOI: 10.1126/science.abj2890

The PDF file includes:

Other Supplementary Material for this manuscript includes the following:

Materials and Methods

Mayo Clinic cases and controls

Mayo Clinic glioma cases have been previously described (*3-6, 45-47*). Controls were obtained from Mayo Clinic's Biobank and have been previously described (*6, 7*). Germline DNA specimens from 337 *IDH* mutant glioma cases and 446 controls were used for fine mapping experiments. ChIPseq and RNAseq experiments utilized tissue from surgical resections on 83 glioma cases and 9 gliosis cases performed at Mayo Clinic between 1988 and 2017. The age range of the gliosis participants was 30-58 (mean 39±9.3) and the male female ratio was 5:4. The RNAseq age range was 22-84 (mean 45±15.8) and the male female ratio was 41:42. The ChIPseq age range was 22-84 (mean 44±15.6) and the male female ratio was 32:31. Tissue sections from the frozen specimens were reviewed by a neuropathologist to confirm histology and mark tumor location. This study was approved by the Mayo Clinic Office for Human Research Protection. Please see Supplementary Table S4 for details regarding the number of Mayo Clinic cases and controls used for RNAseq, ChIPseq and ChromHMM.

UCSF glioma cases

UCSF glioma cases include participants of the San Francisco Bay Area Adult Glioma Study (AGS). Details of subject recruitment for AGS have been reported previously (*3-6, 45-47*). Germline DNA specimens from 285 *IDH* mutant glioma cases and 222 controls were used for fine mapping experiments. The age range of the controls was 18-89 (mean 53±15.3) and the male female ratio was 116:106. The age range of the cases was 19-83 (mean 41±11.7) and the male female ratio was 160:125. This study was approved by the UCSF Committee on Human Research. Please see Supplementary Table S4 for details regarding the number of UCSF glioma cases.

Haplotypes and Recombination mapping

Risk and ancestral non-risk haplotypes were constructed using phased genotyping data for SNPs from 503 EUR subjects from the 1000 Genomes project. SNPs with an alternate allele frequency <0.05 in the EUR population were excluded. Data from linked-read (10X Genomics) sequencing for 6 individuals confirmed the presence of both computed haplotypes in cases and controls (see following section for linked-read sequencing methods). Additionally, no rearrangements or novel variants were identified within the minimal association region using the 10X Genomics data.

Genotyping data from a modified Illumina OncoArray was used to genotype germline DNA from 622 *IDH* mutant glioma cases and 668 controls (*6, 7*). Haploview (https://www.broadinstitute.org/haploview/haploview) was used to examine the haplotype structure of the region surrounding rs55705857. Guided by the Haploview results, subjects carrying the risk haplotype were identified and the genotyping data for these cases was manually examined to identify meiotic crossovers that disrupted the risk haplotype. *IDH* mutant cases and controls heterozygous for the risk haplotype that did not contain crossovers within the region were not included (n = 155 and 45, respectively). Subjects homozygous for the risk haplotype (n = 15 all of which are *IDH* mutant cases) and cases and controls not containing the risk haplotype within this region (n = 397 and 601, respectively) were also not included. The age range of the IDHmut cases was 18-83 (mean 41±11.7) and the male female ratio was 201:136. The age range of the controls was 22-84 (mean 55±14.7) and the male female ratio was 160:125.

Linked read sequencing using 10X Genomics Platform

DNA for five subjects was extracted from 200 µl of snap frozen buffy coats using Qiagen's MagAttract HMW kit Further enrichment for long DNA fragments using the Blue Pippin system and library preparation using the 10X Genomics platform to prepare sequencing libraries was performed by GENEWIZ. The libraries were sequenced on Illumina HiSeq to ~30 fold coverage, data were processed through the 10X Genomics pipeline and the resulting data examined using the Loupe browser 2.1.1 ((https://support.10xgenomics.com/genome-exome/software/downloads/latest). Our analysis also included

the sequencing data for a CEU subject, NA12878, that carries the rs55705857 G allele (Loupe file provided by 10X Genomics).

Frozen Glioma RNA sequencing

Frozen glioma or gliosis samples were crushed in a liquid nitrogen-chilled Cellcrusher™ tissue pulverizer (Cellcrusher, Portland, OR) and transferred to QIAzol Lysis Reagent prior to extraction with the RNeasy Lipid Tissue Mini Kit (Qiagen) per manufactures guidelines. Isolated RNA was DNase treated, ribo-depleted with the Ribo-Zero rRNA removal kit (Illumina). RNA integrity was assessed with the Agilent Tapestation. Samples were sequenced on the Illumina HiSeq in a 2x150bp configuration with a single index.

Frozen Glioma Chromatin immunoprecipitation-sequencing (ChIP-seq)

ChIP-seq was performed as previously described (*48*). Briefly, about 100 mg of frozen tumor or gliosis tissues were homogenized in PBS buffer. The homogenates were fixed to final 1% formaldehyde for 10 minutes at room temperature, quenched with 125 mM glycine for 5 minutes at room temperature, and followed by washing with TBS buffer. The homogenized pellets were resuspended in cell lysis buffer (10 mM Tris-HCl, pH7.5, 10 mM NaCl, 0.5% NP-40) and incubated on ice for 10 minutes. The lysis step was repeated. The lysates were divided into 2 tubes and washed with the MNase digestion buffer (20 mM Tris-HCl, pH7.5, 15 mM NaCl, 60 mM KCl, 1 mM $CaCl_2$). After resuspending in 250 µl of the MNase digestion buffer with proteinase inhibitor cocktails, the lysates were incubated in the presence of 1,000 Gel units of MNase (NEB, M0247S) at 37°C for 20 minutes with continuous mixing in thermal mixer (Fisher Scientific, 05-450-206). The reaction was stopped by adding 250 µl of 2X ChIP buffer (100 mM Tris-HCl, pH 8.1, 20 mM EDTA, 200 mM NaCl, 2% Triton X-100, 0.2% sodium deoxycholate). The chromatin was further sonicated using a Bioruptor sonicator (Diagenode, Denville, NJ) by 30 cycles (30 s on and 30 s off) and soluble chromatin was isolated by centrifugation (21,130 x g, 10 min). Chromatin input was incubated with the antibodies against $H3K4me^1$ (CST, Cat# 5326, Lot 1), $H3K4me^3$ (EDL, Lot 1), H3K27ac (CST, Cat# 8173, Lot 1), or $H3K36me^3$ (Active motif, Cat# 61101, Lot 32412003) overnight at 4 °C and precipitated using Protein G-magnetic beads (GE Healthcare Life Sciences, Pittsburgh, PA). The beads were extensively washed with ChIP buffer, high salt buffer, $LiCl_2$ buffer, and TE buffer. Bound chromatin was eluted and reverse-crosslinked at 65°C overnight. DNAs were purified using Min-Elute PCR purification kit (Qiagen) after treatment of RNase A and proteinase K. The enrichment was analyzed by targeted real-time PCR in positive and negative genomic loci. The size of input chromatin was determined using an Advanced Analytical Technologies (Ankeny, IA) Fragment Analyzer™ Automated CE System. The libraries were prepared from 1 - 10 ng of ChIP and input DNAs with the ThruPLEX DNA-seq Kit (Rubicon Genomics, Ann Arbor, MI) and were sequenced (paired-end; 51 bases/read) on the Illumina HiSeq 4000 platform in the Mayo Clinic Medical Genomics Core.

RNAseq preprocessing and statistical analysis

MAP-RSeq workflow was used to process the RNA sequencing data (*49*). STAR (*50*) was used to align reads to the reference human genome, build hg38. Gene and exon expression quantification was performed using the Subread package (*51*) to obtain both raw and normalized (RPKM – Reads Per Kilobase per Million mapped) reads. Comprehensive quality control analyses from the RSeQC (*52*) package was used to assess the quality of the sequenced libraries. Analysis of differential expression of the gene counts by rs55705857 and tumor/tumor comparisons was performed using the R package edgeR and were considered significant if $p<0.01$ (*53, 54*). Unsupervised hierarchical clustering was performed using the R package heatmap3 (*55*). Both human and mouse samples were included in the clustering. The clustering was limited to transcripts included in both the human and mouse sequencing. Analysis of differential expression was performed between mouse and human samples using edgeR and transcripts that were significantly different ($p<0.01$) were removed. The median absolute deviation was then calculated on the RPKM value of the remaining transcripts and the log of the top 1000 most variable transcripts were used for the clustering. One minus the Pearson correlation coefficient was used as the distance metric for the clustering. TCGA LGG RNAseq data was downloaded from the *recount2* online resource (*56*). Analysis of differential

expression of the TCGA data was performed by rs55705857 and tumor/tumor using edgeR and results were compared to the analysis of the Mayo data to determine which transcripts validated.

TCGA ATAC-seq Analysis

ATAC-seq data (bigwig-files with per base coverage across GRCh38 reference genome) for LGG (13 samples), GBM (9 samples) and SKCM (13 samples) were taken from TCGA (*16*) (https://gdc.cancer.gov/about-data/publications/ATACseq-AWG). We stratified the LGG and GBM samples based on their *IDH* mutation status and subdivided the *IDH* mutation samples further based on presence of 1p-19q co-deletion. The molecular and copy number information were taken from published data (*57*). In LGG cancer type, 1 sample has *IDH*-WT, 7 samples have *IDH*-mut non-codeletion and 5 samples has *IDH*-mut codel. For GBM cancer type, 8 samples have *IDH*-WT and 1 sample has *IDH*-mut non-codel.

Please see Supplementary Table S4 for details of the utilized ATAC-seq data from TCGA.

Analysis of differential binding analysis was conducted to compare the peaks between groups. Samples were grouped based on their *IDH* status from LGG and GBM cancer type. Comparison was done between *IDH*-WT vs *IDH*-Mut. DiffBind (*58*) program was used for this analysis and within this DESEQ2 (*59*) method is used to compare the peaks for finding the differentially bound sites between compared groups.

Human Chromatin immunoprecipitation sequencing (ChIP-seq) data analysis (histone mark peak calling, diffbind, ChromHMM)

ChIP-seq data were analyzed using the Mayo Clinic HiChIP workflow (*60*). Specifically, 51mer, paired-end reads were first analyzed for quality using FASTQC (https://www.bioinformatics.babraham.ac.uk/projects/fastqc/) and then aligned to the human reference genome (GRCh38/hg38) using BWA (version 0.7.17-r1194). The resulting BAM files were sorted and indexed with Samtools (version 0.1.12a) (*61*). PCR and optical duplicated reads were marked and removed using Picard tools (version 1.67) (https://broadinstitute.github.io/picard/). Narrow peaks (H3K4me^1, H3K4me^3, H3K27ac) were called by MACS2 (version 2.0.10.09132012) with q-value cutoff 0.01 (*62*). Broad peaks (H3K36me3) were called by SICER (version 1.1) with FDR cutoff 0.01 (*63*). CEAS and GREAT were used to visualized and annotate (*64*, *65*). FRiP (fraction of reads in peak) score was calculated using deeptools (*66*). BigWig files were generated for visualization with the UCSC genome browser or IGV.

ChromHMM analysis was performed on 4 histone marks (including H3K4me^1, H3K4me^3, H3K27ac, and H3K36me^3) of 77 patients (*67*). Duplicate reads in the BAM files were collapsed. Binarization was performed on BAM files of ChIP samples and the corresponding input controls were used as additional features to adjust the local binarization threshold. We set the '-f' to 3, and used the defaults for other options. During model learning, we set 'numstates' to 8. BigBed files were generated to visualize the chromatin states of each patient.

A total of 10 differential binding analyses were performed for each of the four histone marks (https://bioconductor.org/packages/release/bioc/html/DiffBind.html). Differential peaks were called based upon a p-value less than 1e-5 with a log2 fold change with absolute value greater than 1. Differential peaks were annotated and assigned to the putative target genes by the HOMER (v4.10) (*68*).

Animals

Equal numbers of male and female animals were Equal numbers of male and female animals were used throughout the study without any bias, with the exception of transgenic mouse embryos, which included male and female embryos, but were not examined/scored separately by sex. Animal husbandry, ethical handling of mice and all animal work were carried out according to guidelines approved by Canadian Council on Animal Care and under protocols approved by the Toronto Centre for Phenogenomics Animal

Care Committee (18-0272H). All mouse work performed at Lawrence Berkeley National Laboratory was reviewed and approved by the Lawrence Berkeley National Laboratory Animal Welfare and Research Committee. The animals used in this study were LSL-*Idh1*^{R132H}, kindly provided by Dr. Tak Mak and described previously (*19*, *69*)), R26-LSL-Cas9-GFP (JAX #026175), *Trp53*$^{LSL\text{-}R270H}$ (#129S-Trp53$^{tm3Tyj/J}$, JAX #008651), *Trp53*$^{fl/fl}$ (Trp53^{tm1Brn}, JAX #008462), *Pten*$^{fl/fl}$ (Pten$^{tm1Hwu/J}$, JAX #006440) obtained all from Jackson laboratories. *Atrx*$^{fl/f}$ mice (Atrx^{tm1Rjg}, MGI ID: 3528480) were kindly provided by Dr. David Picketts. *Notch1*$^{fl/fl}$ mice were described previously (*70*). The rs557$^{A->G_4bp}$ and rs557^{66bp} mutant lines were generated in the Toronto Centre for Phenogenomics. Genotyping was performed by PCR using genomic DNA prepared from mouse ear punches.

Animals were randomized by crossing IDH heterozygous mice giving rise to 50% of Idh1 R132H mutant mice and 50% of WT control mice. Mice were randomized for injected with LV-Cre harboring sgAtrx or sgSCR at p1. Mice were randomized for injected with LV-Cre harboring sgAtrx or sgSCR at P1 before genotyping at P21. As such, the experimental procedure was done before the genotype was known. Experiments and histology were collected and analyzed by different people without knowing the genotypes. Mice dying of hydrocephalus within 21 days after birth were excluded.

Enhancer-reporter assays in mouse embryos

A human hs1709 enhancer (chr8:129,631,847-129,635,071; hg38; 3225 bp) containing the reference or the variant allele was PCR-amplified from DNA from the 1000 Genomes Project and cloned into the PCR4-Shh::lacZ-H11 plasmid (Addgene plasmids #139098) upstream of a minimal *Shh* promoter and *lacZ* or an mCherry reporter gene (*18*). The HG00310 DNA sample for PCR amplification of the variant allele was obtained from the NIGMS Human Genetic Cell Repository at the Coriell Institute for Medical Research. We used a mouse enhancer-reporter assay that relies on site-specific integration of a transgene into the mouse genome (*18*). Transgenic assays were performed in the FVB mouse strain. Embryos with integrated enhancer-reporter transgene were collected and LacZ-stained at two time points, E11.5 and E14.5. Embryos were excluded from further analysis if they did not carry the reporter transgene integrated at the H11 locus. All embryo images for the reference and variant alleles of hs1709 enhancer were randomized, the labels removed, and annotation was performed by at least four independent reviewers blinded to the genotype. For each embryo, reviewers scored whether the enhancer activity pattern in each tissue was 1) robust, 2) weak, or 3) absent. Final annotations were determined by the staining type with the most reviewer votes. E14.5 mCherry reporter embryos were sections and stained with the following antibodies mCherry (Fisher Scientific, PA5-34974) and SOX2 (Santa Cruise, SC-17320), TUJ1 (Biolegend, 801202), CTIP2 (Abcam, AB18465), GFAP (Millipore, AB5541), OLIG2 (R&D, AF2418), MAP2 (Abcam, AB5392), SATB2 (Abcam, AB51502) and S100β (SigmaS2532).

Generation of mice with mutations in the homologous rs55705857 loci

The human genomic sequence surrounding rs55705857 was aligned with the syntenic regions of the mouse and human genome to identify the target nucleotide. The target A nucleotide is conserved between mouse and human and adjacent sequences are only slightly divergent:

```
Human 8:129633407    ATGAGGAATTCCAAGGACTTG-CTCAGAAGCCGTTCTGCARATGCATTTCTTGAACAAAG
Mouse 15:63675539    ATGAGGAATTCCAAGGACTTAACTCAGAAGCCGCTCTGCAAATACATGGCTTGAACAAAG
                     ********************. *********** ****** **.*** ***********
```

The desired allele is a A>G mutation at Chr15:63675579. Sequence analysis of the ~70 bp surrounding this site in genomic DNA revealed gRNAs sequence with predicted endonuclease sites at or near Chr15:63675579. These gRNA sequences were scored for specificity (*71*). Using this prediction algorithm, gRNA_ag appears to have a suitable target endonuclease site – 2 bp from Chr15:63675579 – with good specificity. All putative off-target sites have at least 3 mismatches

gRNA	Sequence	Location (Strand)	Specificity Score	No. off-target sites	
				Total	In genes
gRNA_ag	GAAGCCGCTCTGCAAATACA	Chr15: 63675565 (+1)	72	172	17

The specificity score of each gRNA is predicted to reflect the faithfulness of on-target activity and is calculated as 100% minus a weighted sum of off-target site scores in the target genome (Mus musculus) (http://crispr.mit.edu/about). The off-target site scores are calculated using an algorithm that takes into account the experimentally determined effect of gRNA:target DNA mismatches. Using Cas9 to create mutations in mouse zygotes demonstrated an undetectable off-target rate for gRNAs with ≥3 mismatches at all putative off-target sites (0 off-target mutations from among the top 8-10 scoring off-target sites for 64 different gRNAs screened in 207 N1 mice – a total of 3,060 loci were screened). We used a repair template will be a single-strand oligonucleotide encoding the A>G change (red boldface):

TTGGCACGGTCCTAATGACTTAAAGAAAATGCCGGAAACCAGCCCCGCACTCTTTTCTGAAAGGAACATTGGCCCTTTGTTCAA
GCCATGTAT**C**TGCAGAGCGGCTTCTGAGTTAAGTCCTTGGAAT

This mutation introduces a single base-pair change in the seed region of the gRNA, but does not disrupt the protospacer adjacent motif (PAM). The oligonucleotide is antisense to the PAM-containing strand and in an asymmetric oligonucleotide design to improve repair frequency (*72*).

The CRISPR/Cas9 sgRNA RNP was inject WT B6J zygotes and targeted founder mice were identified using sanger sequencing of a 344bp PCR amplicon encompassing the homologous rs55705857 locus using the rev. primer (fwd. primer: GAAAGCCCTTGCTTCTTCAATAC and rev. primer: CTGTCTGTAGCCACCATCAATAA). Two founder alleles were identified (Figure S6C) and backcrossed three times to B6J mice before intercrossing to the experimental *Idh1*$^{LSL\text{-}R132H/+}$;*Atrx*$^{fl/fl}$;*Trp53*$^{fl/fl}$;R26-Cas9 mice.

Lentiviral constructs

All the sgRNAs targeting gene of interest were cloned into pLKO-Cre stuffer v4 plasmid (Addgene #158032) (*73, 74*) by using BsmBI restriction sites. sgRNAs targeting genes found mutated in LGG and non-targeting sgRNAs were ordered as oligos from IDT (sgAtrx #1: CTTGTCATGAACCAAAGCAC, sgAtrx #2: GTGCTGAATGAAGACAAAGA) and cloned into pLKO-Cre stuffer v4 using BsmBI restriction sites.

Lentivirus production and transduction

Large-scale production and concentration of lentivirus were performed as previously described (*73, 74*). 293T cells (Invitrogen R700-07) were seeded on a poly-L-lysine coated 15 cm plates and transfected for 8 hours using PEI (polyethyleneimine) method in a non-serum medium with lentiviral construct of interest along with lentiviral packaging plasmids psPAX2 and pPMD2.G (Addgene #12259 and 12260). Post transfection, medium was added to the plates supplemented with 10% Fetal bovine serum and 1% penicillin-streptomycin antibiotic solution (w/v). 48 hours after transfection, viral supernant was filtered through a Stericup-HV PVDF 0.45-μm filter, and then concentrated ~2,000-fold by ultracentrifugation in an MLS-50 rotor (Beckman Coulter). Viral titers were determined by FACS based quantification of infected R26-LSL-tdTomato MEFs.

Adenoviral constructs

Adenovirus (Ad-Cre and Ad-GFP) was ordered from University of Iowa Viral Vector Core Facility.

Intercranial injection and lentiviral transduction

As previously described (*75, 76*), virus was mixed with 0.05% Fast Green (F7252-5G) and loaded into a syringe (Hamilton 7659-01) with 33-gauge needle (Hamilton 7803-05). P0 pups were anesthetized on parafilm covered ice and their head secured with a custom 3D-printed mold. A stereotactic manipulator was used to position the needle to 0.3 mm above the Bregma towards the Lambda Suture and 0.1 mm lateral of Sagittal Suture into the right ventricle. The needle punctured 3 mm into the skull, and retracted 1mm for a final depth of 2 mm. 1 μl of virus was administered and allowed 1 minute to diffuse before retraction of the needle. Post-injection, the neonates were warmed by cupping them in hands until conscious.

2HG-Sample quantification

One 10 cm plate of confluent *Idh1*$^{LSL\text{-}R132H/+}$ primary NSC or 500mg brain tissue of *Idh1*$^{LSL\text{-}R132H/+}$ mice transduced with either Ad-GFP or Ad-Cre-GFP was harvested, pelleted and snap frozen at -80 °C. Samples were analyzed by LC/MS/MS at the Analytical Facility for Bioactive Molecules (The Hospital for Sick Children, Toronto, Canada). Sample extraction was prepared based on published method (*9*) with slight modifications. Briefly, 200 µL of ultrapure water were added to cell pellets. Samples were sonicated for 1 minute on ice (550 Sonic Dismembrator, Fisher Scientific). 20 µL were transferred into a set of 1.5 mL Eppendorf tubes and volume was adjusted to 200 µL with ultrapure water. 800 µL methanol were added, samples were mixed by vortex for 5 minutes and kept on ice for 15 minutes. After centrifugation (20,000 g, 15 minutes at 4°C) to remove precipitated proteins, supernatants were dried under a stream of nitrogen. Residues were reconstituted in 200 µL methanol/water (1/1) and after centrifugation (20,000 g, 15 minutes at 4 °C), clear supernatants were transferred into a set of 200 µL plastic inserts for LC-MS-MS analysis.

2-HG is measured by liquid chromatography-tandem mass spectrometry using a QTRAP 5500 triple-quadruple mass spectrometer (Sciex: Framingham, Massachusetts, USA) in negative electrospray ionization mode by MRM data acquisition with an Agilent 1200 HPLC (Agilent Technologies: Santa Clara, California, USA). Chromatography is performed by automated injection of 5 µL on a Synergi hydro RP column, 150 x 2 mm, 4.0 µm particle size) (Phenomenex, Torrance, CA). The HPLC flow is maintained at 300 µL/minute with a gradient consisting of: A= 10 mM ammonium acetate, pH 3.2 and B = methanol. Total run time was 10 minutes.

R/S-2HG quantification

Quantification was done on Analyst 1.6.1 software (ABSciex : Framingham, Massachusetts, USA) by plotting the sample peak area ratios (Analyte peak area/Internal Standard peak area) of 2-HG against a standard curve generated from various concentrations of 2-HG from 1 ng to 750 ng, spiked with the same amount of 2-HG-d4 used for the samples and extracted in the same conditions

Metabolomic Profiling by LC/MS

Mouse Neural stem cells 500,000 were seeded in 6-well plates and cultured for 48 hours. Medium was aspirated, cells washed with warmed PBS (Wisent, 311-010-CL) and then snap frozen in liquid nitrogen. Metabolites were extracted by adding 1mL of extraction solvent (40% acetonitrile, 40% methanol and 20% water), scraped and transferred to a 1.5mL tube. Samples were shaken at 4°C at 1400 rpm for 1 hour. Samples were centrifuged and supernatant was placed into a new tube where it was evaporated in a CentreVap concentrator at 40°C. Samples were stored at 80°C for later LC-MS/MS analysis.

Dry extracts were reconstituted in 100ml of water containing internal standards (500 mg/mL and 300 mg/mL of D7-glucose and 13C9 15N-tyrosine). The metabolites were separated at room temperature through a guard column (Inertsil ODS-3, 4 mm internal diameter X 10 mm length, 3 mM particle size) and analytical column (Inertsil ODS-3, 4.6 mm internal diameter, 150 mm length, and 3-mM particle size) for both polarity modes. Eluted metabolites were analyzed at the optimum mass spectrometric conditions as published (*77*). Peaks were manually confirmed in Multiquant (*77*) and area ratio compared to IS was normalized to final cell counts and uploaded for statistical analysis in MetaboAnalyst (*78*).

Tide analysis

LSL-Cas9-GFP MEFs were cultured and infected with lentivirus carrying Cre and corresponding sgRNAs. Cells were live sorted for GFP expression and expanded further to extract genomic DNA using DNeasy Blood & Tissue Kit (Qiagen). Genomic DNA from tumors from the mice injected with single sgRNAs were also isolated using the same kit. PCR was performed flanking the regions of sgRNA on genomic DNA from both WT MEFs and cells infected with respective virus or tumors and sent for Sanger sequencing. Sequenced chromatograms were uploaded to https://www.deskgen.com/landing/tide.html and genome editing efficiency was estimated.

Western blot analysis

Protein extracts from cell lysates were harvested by adding RIPA lysis buffer directly confluent 6-well cultures of either RIP or mouse NSCs at on ice for 15 minutes. Cell lysates were then transferred to an Eppendorf and centrifuged at 16,000 g for 15 minutes and supernatant was transferred a new Eppendorf tube. Samples were boiled in loading dye with 1/50 volume 2-Mercaptoethanol for 5 minutes and loaded into a Bolt BisTris Plus 4-12% gradient gel (Life Technologies, NW04127BOX) with Bolt MOPS SDS Running Buffer (Life Technologies, B0001). Protein gels were run for 40 minutes at 200 V, and subsequently transferred to a PVDF membrane (Millipore, IPFL00010) in Tris Glycine buffer (Wisent, 880-560-LL) for 2 hours at 0.3 amps. Western blots were blocked in 5% milk for 1 hour and placed in primary antibody diluted in 5% milk over night at 4°C. Primary antibodies used were 1:1000 diluted $Idh1^{R132H}$ (generous donation of MilliporeSigma, 456R-31), 1:10000 diluted Gapdh (Biolegend, 607904), 1:1000 diluted OCT2 (Life Span Biosciences, LS-C124305-100) and 1:1000 diluted Oct4 (Abcam, ab181557). All blots were washed with PBS and then placed in Goat Anti-Rabbit IgG HRO (Bio Rad, 1706515) diluted 1:10000 in 5% milk for 1 hour. Blots were washed with PBS before adding 500 µl of Clarity Western ECL Substrate (Bio Rad, 1705061) and imaging on a Bio Rad ChemiDoc XRS+.

Mouse brain tissue histology

Mice were euthanized by CO2 asphyxiation, brains were dissected and submerged in 10% buffered formalin for 2-3h, then cut midline sagittal, and continued fixation for at least 48h, after which they were transferred to 70% ethanol and subsequently processed and embedded in paraffin following standard procedures. Brains were oriented in a "butterfly" pattern and sections cut with two sections per slide for staining. Prior to staining, slides were heated at 60°C for 15 minutes, then dewaxed and rehydrated. Slides for immunohistochemistry were treated with 3% hydrogen peroxide in PBS for 15 minutes to kill endogenous peroxidases. (For the x-Nestin antibody to work required killing of endogenous peroxidases with 10% H2O2 in 70% MeOH.) Slides were then washed in PBS followed by microwave antigen retrieval using NaCit (pH6) or TRIS-EDTA (TE, pH9). Only x-GFAP antibody did not require AgRet. The following markers and conditions were used to evaluate our thesis: $IDH1^{R132H}$ (generous donation of MilliporeSigma, 456R-31), TE/1:400; PDGFRa (R&D AF1062), TE/1:100; Ki67 (Abcam ab15580), NaCit /1:1000; GFAP (Dako Z0334) no AgRet/1:200; OLIG2 (Millipore AB9610), TE/1:500; NESTIN (Pharmingen 556309), TE/1:150; Cleaved Caspase 3 (ASP175 – Cell Signalling Technologies 9661), NaCit/1:750; and p53 (CM5, Vector Labs VP-P956), NaCit/1:1000 and MYC (abcam ab32072), NaCit/1:400. Secondary antibodies (Vector Labs) were diluted in PBS and 0.2% Triton X-100 applied at 1:500, (x-rabbit, BA-1000; x-goat, BA-5000; x-mouse, BA-9200). An ABC kit (Vector Labs, PK-4100) and DAB Reagent (Vector Labs, SK-4100) were used according to the manufacturer's instructions. Primary antibodies were blocked and diluted in a Histoblock solution with 5% serum of the host of the secondary antibody and 0.2% Triton X-100. Primary antibodies were incubated at room temperature for 35-45 minutes, secondary antibodies for 35 minutes, and ABC for 25 minutes. The DAB reaction was allowed to proceed for 2-4 minutes. Slides were counterstained for 8 minutes in Harris Hematoxylin, washed in water, dehydrated, and mounted in a xylene based mounting medium. Stained sections were digitized at 40x using a Hamamatsu Nanozoomer Scanner (2.0-HT).

RNAseq of mouse tumor tissue and GSEA

RNA quality was assessed using an Agilent 2100 Bioanalyzer, with all samples passing the quality threshold of RNA integrity number (RIN) score of >8. The library was prepared using an Illumina TrueSeq mRNA sample preparation kit at the LTRI sequencing Facility, and complementary DNA was sequenced on an Illumina Nextseq platform. Sequencing reads were aligned to mouse genome (mm10) using Hisat2 version 2.1.0 and counts were obtained using featureCounts (Subread package version 1.6.3). Analysis of differential expression was performed using DESeq2 release 3.8. Gene set enrichment analysis was performed using GSEA version 3.0. Samples were processed using the Hallmark gene sets gathered from https://www.gsea-msigdb.org/gsea/msigdb/collections.jsp#H.

Derivation and culturing of mouse tumor cells

Tumor tissue was harvested and washed in HBSS (Wisent, 311-512-CL) before transferred into 10cm plate containing 10 ml TrypLE Express (Life Technologies, 12604021) and incubated for 10 minutes at 37°C. Tumor tissue was then mechanically dissociated with a pipette and transferred to a 50ml conical tube with 40ml HBSS. Samples were centrifuged at 300xg for 5 minutes, supernatant was transferred to a new 50ml conical tube and centrifuged at 300xg for 5 minutes. Both cell pellets were pooled and washed with 40ml of HBSS. The pellet was resuspended in Tumor Stem Medium Base Formulation (Wisent, 305-485-CL) and seeded into 6-well plates +/- 2uM AG120.

Mouse Tumor cells were cultured in at 37°C, 5% O_2 and in Tumor stem medium base formulation supplemented with 1X concentration W21 (Wisent, 003-017-XL), 1X concentration N2 (Wisent, 305-016-IL), 20 ng/mL H-EFG (Wisent, 511-110-EU), 20 ng/mL H-FGF basic (Wisent, 511-126-EU), 10 ng/mL H-PDGF-AA (Shenandoah, 100-16-100UG), 10 ng/mL H-PDGF-BB (Shenandoah, 100-18-100 μg) and 2 μg/mL heparin solution (Stem cell technologies, 07980). Cells were passaged using TrypLE Express.

OCT2/4 ChIP-PCR / RT-PCR

Chromatin Immunoprecipitation was performed with the SimpleChIP Enzymatic Chromatin IP Kit (#9003, Cell Signaling Technology) according to the manufacturer's protocol with minor modifications. Cells cross-linking for ChIP: Confluent 10 cm plates of RIP cells and RIP cells treated with OCT4 were used for each experiment. Cells were cross-linked while in medium with 270 μL of 37% formaldehyde. Following a 10 min incubation at room temperature, 1 mL of 10X glycine was added to each plate. After 5 minutes of incubation at room temperature, cells were washed twice with ice cold PBS and scraped into cold PBS buffer containing protease inhibitor cocktail. Harvested cells were frozen in -80°C until all samples have been processed before starting the next step. Chromatin extraction: Cross-linked cells were thawed on ice and resuspended in 1 mL cold Buffer A, mixed well, and centrifuged at 2000x g for 5 minutes at 4°C. The pellet was then mixed in 1 mL cold Buffer B, incubated on ice for 10 minutes, then centrifuged at 2000xg for 5 minutes at 4°C. After resuspension in Buffer B, chromatin was digested with 0.5 μL MNase for 20 minutes at 37°C, using a Thermomixer at 850 rpm. Finally, the reaction was stopped by the addition of 10 μL 0.5 M EDTA, and the tubes were then placed on ice for 2 minutes. The cells were then pelleted and resuspended in 400 μL cold ChIP buffer, and sonicated on ice using a 3.2 mm microtip with QSonica Q700 (25% amplitude, 10 seconds on, 15 seconds off) for a total of 3 cycles to release the chromatin. All the lysates were centrifuged at 9400x g for 10 minutes at 4°C. The supernatant was collected and total chromatin quantified as per kit instructions before the start of each immunoprecipitation (IP). Immunoprecipitation: Total digested chromatin was diluted accordingly to a total volume of 500 μL, with 2 ug of chromatin per IP, in cold ChIP Buffer. Each ChIP sample was precleared by incubating with 30 μL of Protein G magnetic beads, at 4°C with rotation for 1 hour. Samples were then incubated with the appropriate antibody (2 ug per IP) at 4°C overnight with rotation. We prepared MNase ChIP-seq data using the following antibodies: H3K4me[1] (ab8895, Abcam, lot: GR3312607-1), H3K27ac (ab4729, Abcam, lot: GR3187598-1), OCT4 (ab181557, Abcam, lot: GR3236296-3), SOX2 (AF2018-SP, R&D Systems, lot: KOY0419061) and OCT2 (C124305, LifeSpan BioSciences, lot: 167932). OCT4 antibody (sc9081, Santa Cruz, Lot: B0113) was used for human cells. All buffers and solutions, including antibodies against total histone H3 protein (H3KPan) and normal rabbit IgG, were provided by Cell Signaling Technology (#9003 Simple ChIP kit). On the following day, 30 μL of Protein G magnetic beads were added to each sample and then further incubated at 4°C with rotation for 2 hours. After incubation, samples were placed on a magnetic rack and washed three times with 1 mL Low Salt Wash Buffer for 5 minutes at 4°C with rotation, then washed once with High Salt Wash Buffer for 10 minutes at 4°C with rotation. The remaining beads were resuspended in 150 μL Elution Buffer and incubated in a Thermomixer at 1200rpm for 30 minutes at 65°C. The eluted fractions were then treated with 6 μL 5M NaCl and 2 μL Proteinase K, and incubated overnight at 65°C to reverse the cross-linker. Finally, samples were cleaned up according to manufacturing instructions and purified samples were used for further analysis. Quantification by RT-PCR and PCR: A set of primers were specifically designed to flank the cassette insertion region in the targeting homologous mouse rs557055857 locus (Fwd: 5'-ACCGGGAGCTTACAAAGACA-3', Rev: 5'-

ACATTGGCCCTTTGTTCAAG-3'). The same primer set was used for both RT-PCR and PCR quantification. The WT product size is 117bp, whereas the rs557 knock out product size is 51bp. For human LGG lines, we used (Fwd: 5'-TTCTTCAATGCCAGGAGCTT-3', Rev: 5'-AAAGAAAAATGCCGGAAACC-3'). A mastermix was created as follows: 3 μL nuclease-free water, 5 μL 2X PowerUp SYBR Green Master Mix (A25742, Applied Biosystems, lot: 00828561), 1 μL of 5 μM rs557 primer mix and 1 μL of purified DNA. For PCR, samples went through the PCR reaction program according to manufacturing instructions with a total of 35 cycles and products were ran on a 2.5% gel. Enrichment over IgG was calculated by using threshold cycles for each sample normalized to the IgG control after setting the input value at 2%.

MYC-ChIP-Sequencing

Frozen patient tumor samples were submerged in liquid nitrogen and homogenized manually with a mortar and pestle for 5 minutes until no visible chunks remained visible. Next, samples were transferred into 15mL conical tubes on dry ice with lids off to allow for the liquid nitrogen to evaporate. Samples were then fixed at room temperature for 20 minutes in 4 mL solution (1% formaldehyde, 50 mM Hepes-KOH, 100mM NaCl, 1mM EDTA, 0.5mM EGTA). To quench the formaldehyde, 200 μL of 2.5M glycine was added into each sample, incubated at 5 minutes at room temperature. Samples were then washed twice with ice cold PBS (4°C, 2000 x g for 5 minutes per wash). Finally, the samples were processed according to the ChIP protocol as discussed above, but with 10ug of chromatin used per IP reaction instead. ChIP antibodies on the patient tumor samples were anti-c-Myc (N262, generous gift from Dr Linda Penn) and anti-c-Myc (abcam, #ab32072, lot# GR337768-4). ChIP DNA samples were sequenced using the NovaSeq S4 flowcell (Illumina) with paired end reads.

CRISPR interference

IPO cells were transduced with low-titter virus expressing dCas9 protein and blasticidin resistance (Addgene: Plasmid #89567) and centrifuged at 37°C at 1100xg for 1 hour. Cells were recovered for 48 hours post transduction before undergoing blasticidin selection for one week. After blasticidin selection (Wisent, 450-190-XL), IPO dCas9 cells were transduced with pLKO puromycin resistance sgrs557 or sgNTC constructs and underwent puromycin selection (Wisent, 450-162-XL) for one week. Cells were then cultured without selection and harvested for RT-PCR.

qRT-PCR

RNA samples were purified from cells using either Trizol (Life Technologies) or Quick-RNA Microprep Kit (Zymo Research), treated with DNase I (Zymo Research), and reverse transcribed into cDNA using SuperScript IV VILO (Invitrogen). Primers were designed to span exon junctions using Primer3Plus. Primers used are shown in Supplemental Table X. Primers were validated against a standard curve and relative mRNA expression levels were calculated using the comparative Ct method normalized to the housekeeping mRNA. Real-time quantitative PCR (qRT-PCR) reactions were performed in 384-well plates containing 12.5 ng cDNA, 150 nM of each primer, and 5 μl of SYBR Green in a 10 μL total volume reaction. 2X SensiFAST SYBR No-ROX kit (Bioline) was used with the CFX384 system (Biorad) and PowerUP SYBR Green Master Mix (Applied Biosystems) was used with the QuantStudio 5 (Applied Biosystems). The cycling time used was as per manufacturing protocol to the respective SYBR Green, and each reaction was performed in technical triplicates. Please see Supplementary Table S4 for details regarding RT-PCR primers.

OCT4 (Pou5f1) overexpression cell lines

Mouse RIP LGG cells were transduced with pLEX306-Oct4V5-Cre and Oct4 expression was monitored through Western blot Analysis 48 hours post transduction. After 24hr, cells were fixed directly on the cell culture plate with 1% formaldehyde processed for ChIP.

Circular Chromosome Conformation Capture -Seq

Neural stem cells were cultured in 10cm plates and crossed linked with 1% PFA for 10 minutes and subsequently quenched with 2.5 M glycine and washed with PBS. 4C-seq was performed using a modified version of the 4C-seq protocol as previously described (*79*). Briefly, cell pellets were incubated on ice for 15 minutes in lysis buffer (10mM Tris-HCl pH 8, 10mM NaCl, 0.2% Nonidet P-40 and 1x protease inhibitor). Pellets were then centrifuged at 2500G at 4°C, the supernatant discarded, resuspended in 50 µl of 0.5% SDS and incubated at 62°C for 10 minutes. 170 µL of 1.47% Triton™ X-100 was added and samples were incubated at 37°C for 15 minutes. The first digestion was performed using 200U DpnII (NEB R0543L) overnight at 37°C and 700rpm. Samples were heat inactivated at 65°C and cooled to room temperature. In-situ ligation was performed at RT for 15minutes on a rotator using high concentration T4 DNA Ligase (NEB, M0202M), pelleted and resuspended in 550 µL 10mM Tris buffer pH 7.5. Chromatin was reverse-crosslinked by addition of 50 µl 20mg/ml proteinase K and 57 µl of 10%SDS at 55°C for 30 minutes. 67 µL of 5M NaCl was added to the samples and incubated for 1 hour at 68°C. DNA was purified using the 0.8X AmpureXP clean up (Beckman Coulter, A63880). The second digestion was performed with addition of 20U NlaIII (NEB R0125L) for 2 hours at 37°C at 700 rpm and was subsequently heat inactivated at 65°C. The second ligation was performed at 16°C overnight under dilute conditions in a total volume of 5mL per sample. DNA was then purified by adding 0.1X volume of sodium acetate, 0.7 volumes of isopropanol, 2 µL of 5 µg/µL Linear-polyacrylamide (Thermoscientific, AM9520) and 2 µL glycoblue (Fisher Scientific, AM9515) overnight at -80°C. DNA was washed with 70% ethanol, air dried, resuspended in 200 µL 10mM Tris buffer pH 7.5 and purified using 1.8X AmpureXP clean up protocol.

Primers targeting Myc were designed using the 4C primer designer (https://mnlab.uchicago.edu/4Cpd/). Illumina-compatible adapter sequences were appended to Viewpoint-specific primers (bold).

Myc-upstream-reading: TCCCTACACGACGCTCTTCCGATCT**TAGACCTCATCTGCGGTTGATC**

Myc-upstream-nonreading:
GTGACTGGAGTTCAGACGTGTGCTCTTCCGATC**AAAATCAAGGCGCTAGACGC**

4C PCR was performed as previously described (*79*) using the Expand Long Template PCR System (Sigma, 11681834001) and purified using Zymogen DNA Clean & Concentrator (Zymogen, D4003). NEBNEXT adaptors and barcodes were added using PCR amplification and the samples submitted for Illumina sequencing. 4C-seq libraries were obtained in fastq format and filtered for reads containing 4C primer sequences for Myc with an edit distance of <=2. Analysis and visualization of the resultant filtered reads was performed using 4Cseqpipe (*79*). Only R1 reads were used.

For domainograms, the black trendline shows the median contact frequency in 2-kb windows tiled across 1-kb increments normalized to the maximum median value at 2-kb resolution; shaded area indicates the 20th to 80th percentiles. The heat map color-scale shows median contact frequency in the windows of increasing size from 2 to 50 kb tiled across 1-kb increments, normalized relative to the maximum median value at 12-kb resolution.

Generation of Glioma MYC Gene Sets

We used two approaches to generate lists of genes regulated by MYC in gliomas. The first approach used existing expression data from The Cancer Genome Atlas (TCGA) lower grade glioma (LGG) study to identify genes correlated to MYC expression. Our second approach used MYC ChIPseq to identify genes with MYC bound to the gene's promoter region.

Normalized expression data for the TCGA-LGG study were downloaded from the Broad Institute (https://gdac.broadinstitute.org/runs/stddata__2016_01_28/data/LGG/20160128/; downloaded on 4/17/2022, while clinical and mutation data from the TCGA Pan Cancer study were downloaded from CBioPortal (https://www.cbioportal.org/ downloaded on 4/17/2022). Data from primary tumor samples were retained while recurrent specimens and those not classifiable into one of the three major 2021 World Health Organization's (WHO) adult diffuse glioma molecular groups (IDH mutant, 1p/19q codeleted; IDH mutant 1p/19q, non-codeleted; or IDH wild type) were removed. Within each of these three molecular groups, the Pearson correlation coefficient between MYC and all other genes was calculated and genes with correlation coefficients >0.4 or <-0.4 were placed in gene sets positively correlated and negatively correlated to MYC, respectively.

Additional gene sets for IDH mutant, non-codeleted and IDH wild type gliomas were derived from MYC ChIPseq data. Genes identified as regulated by MYC were split into gene sets positively correlated and negatively correlated to MYC using the TCGA LGG data for the corresponding WHO molecular group. A table containing these new gene sets in addition to the MSigDB MYC gene sets can be found in Supplemental Table 3. The overlap between the MYC gene sets was calculated by dividing the number of genes in the intersection by the number of genes in the individual gene sets. The heat map of the overlap can be found in Figure S3.

Gene Set Enrichment Analysis

Gene set enrichment analysis (GSEA) was performed using GSEA version 4.2.3 for Windows, previously published gene sets downloaded from the Molecular Signature Database (MSigDB) version 7.5.1 and the novel gene sets described above for MYC in glioma.

GSEA was performed on RNAseq data from Mayo glioma and gliosis specimens using GSEA pre-ranked lists (*80*). The ranking method utilized a signed F statistic obtained by applying the sign of the log fold change to the F statistic.

GSEA was performed using the Hallmark collection from the MSigDB, a collection of 63 MYC gene set from the MSigDB, and the novel glioma MYC gene sets described above (see Supplemental Table 3). One MYC gene set from the MSigDB, MENSSEN_MYC_TARGETS, contained UNIGENE identifiers that MSigDB did not map to known gene symbols. Gene symbols for this gene set were obtained from the original publication (*81*) (see Supplemental Table 3).

Fifty control gene sets of identical size to our glioma MYC gene sets described above were generated by randomly selecting genes from the TCGA RNAseq data (n=10 for each of the 5 gene sets). GSEA of these gene sets was performed using the RNAseq data for the comparison of rs55705857 G versus A allele in IDH mutant non-codeleted tumors. The best FDR q-value and NES obtained for the control gene sets were 0.022 and 1.62, respectively. Distribution of FDR q-values and NES are shown in Supplementary Figure S21. Only gene sets with an FDR $q \leq 0.05$ in at least one comparison are included and colored in the heat map (Figs 1D and S3), the darker reds and blues have an FDR $q<0.001$.

Genome Architecture Mapping (ImmunoGam)

Publicly available normalized Genome Architecture Mapping (GAM) contact matrices (50kb resolution; GSE148792), insulation scores, and pseudobulk single-cell RNA- and ATAC-seq data were obtained from mouse embryonic stem cells (mESCs), cortical oligodendroglia (OLGs), hippocampal pyramidal glutamate neurons (PGNs), and midbrain dopamine neurons (DNs) (*32*).

For visualization of GAM contact matrices, scale bars were adjusted for a range between 0 and the 99th percentile of normalized pointwise mutual information (NPMI) values for each cell type.

Strong GAM interactions for a single genomic window of interest were determined using an 85th percentile NPMI cutoff for each cell type, based on the distribution of NPMI values within the region of interest with a minimum contact distance of 1 genomic window (chr15:61,500,000-64,500,000). Strong interactions were visualized using a custom python script (*32*).

Human in vitro enhancer-reporter assay

A reporter construct was made that contained 686bp (chr8:129,633,091-129,633,776;hg38) containing the non-risk (A) or risk (G) allele at the rs55705857 locus, and cloned into the c-myc promoter (Del 1) vector (Addgene plasmids #16601) upstream of a myc promoter and firefly luciferase reporter gene. Briefly, 1 × 105 293FT cells were plated in 24-well plates with DMEM medium containing 10% fetal bovine serum, 0.1 mM MEM Non-Essential Amino Acids (NEAA) and 0.5 mg/mL of Geneticin. Cells were transfected with 3 µl of Lipofectamine 2000 (Invitrogen) and 1.5ug of total DNA per well (10:1 ratio of rs55705857 luciferase reporter:Renilla reporter). Luminescence was measured 48 hours after transfections with the Dual luciferase reporter assay system (Promega Corp., Madison, WI). Briefly, the medium was carefully removed, passive lysis buffer was added and rocked for 15 min at room temperature. After the incubation, lysed cells were mixed with firefly luciferase reagent (LARII) and Renilla luciferase reagent sequentially according to the manufactures instructions and measured in luminescence mode on the Tecan SPECTRAFluor Plus. The data are represented as the ratio of Firefly luciferase to Renilla luciferase.

hiPSC lines, maintenance and cerebral organoid differentiation.

The PGP1 cell line was edited at the rs55705857 locus by Synthego to make cells homozygous for the risk (G) allele. Four risk clones were isolated (Clones A5, B5, E3 and C10), and isogenically matched to the PGP1 wt (Synthego, Redwood City, CA) and the GM23338 (ATCC, Manassas, VA) non-risk hiPSC lines. hiPSC cells were grown in feeder-free conditions on hESC-Qualified Matrigel (Corning, corning, NY) in mTeSR Plus medium (StemCell Technologies, Vancouver, Canada).

Cerebral organoid differentiation was performed using the STEMdiffTM Cerebral Organoid Kit (StemCell Technologies). hiPSC were grown in 96-well, round-bottom plates embryoid body (EB) formation medium for 5 days, embryoid bodies were transferred to 24-well plates with neural induction medium. On day 7, the spheres were embedded in matrigel and maintained in expansion medium in 6-well plates for three days. At day 10 the organoids we transitioned to maturation medium and moved to an orbital shaker inside the 37C culture incubator. Organoids were resupplied with maturation medium twice a week until fixation or RNA isolation at 4 weeks.

The organoids were fixed overnight in 4% paraformaldehyde at 4C, and cryoprotected in 15% and 30% until the organoids sank. Organoids were embedded in O.C.T. compound (Tissue-Tek, Torrance, CA) and frozen in a methylbutane bath. They were then cryosectioned for H&E examination (5 µm) or for immunofluorescence staining (15 µm). Frozen tissue sections were blocked (PBS-T + 2% BSA + 0.5% TritonX + 3% normal goat serum) and labeled with Sox2 (R&D Systems, Minneapolis, MN, MAB2018; 1:500) and Pax6 (BioLegend, San Diego, CA, #901301; 1:1000) to confirm cerebral organoid lineage.

Automated IHC HALO analysis

HALO (Indica Labs) was used to quantity MYC expression levels using the Cytonuclear v2.0.9* algorithm. Tumor regions were annotated and then scanned for nuclear staining with the following settings: Stain 1 Mark up color: 137,68,42, Stain 1 Min OD: 0.135,0.3119,0.4903, Stain 1 Mask: not set. Cells detected with the parameters: Nuclear Threshold: 0.0525, Minimum Nuclear Opacity 0.093, Nuclear Size: 5,571.1, Minimum Nuclear Roundness: 0, Nuclear Segmentation Aggressiveness: 0.066, Fill Nuclear Holds: True, Maximum Cytoplasm Radius: 5.

Statistics and reproducibility

All quantitative data are expressed as the mean ± SD. Differences between groups were calculated by two-tailed Student's t-test or one-way analysis of variance using Prism 7 (GraphPad software). $P < 0.05$ denotes significance.

Supplemental figures and figure legends

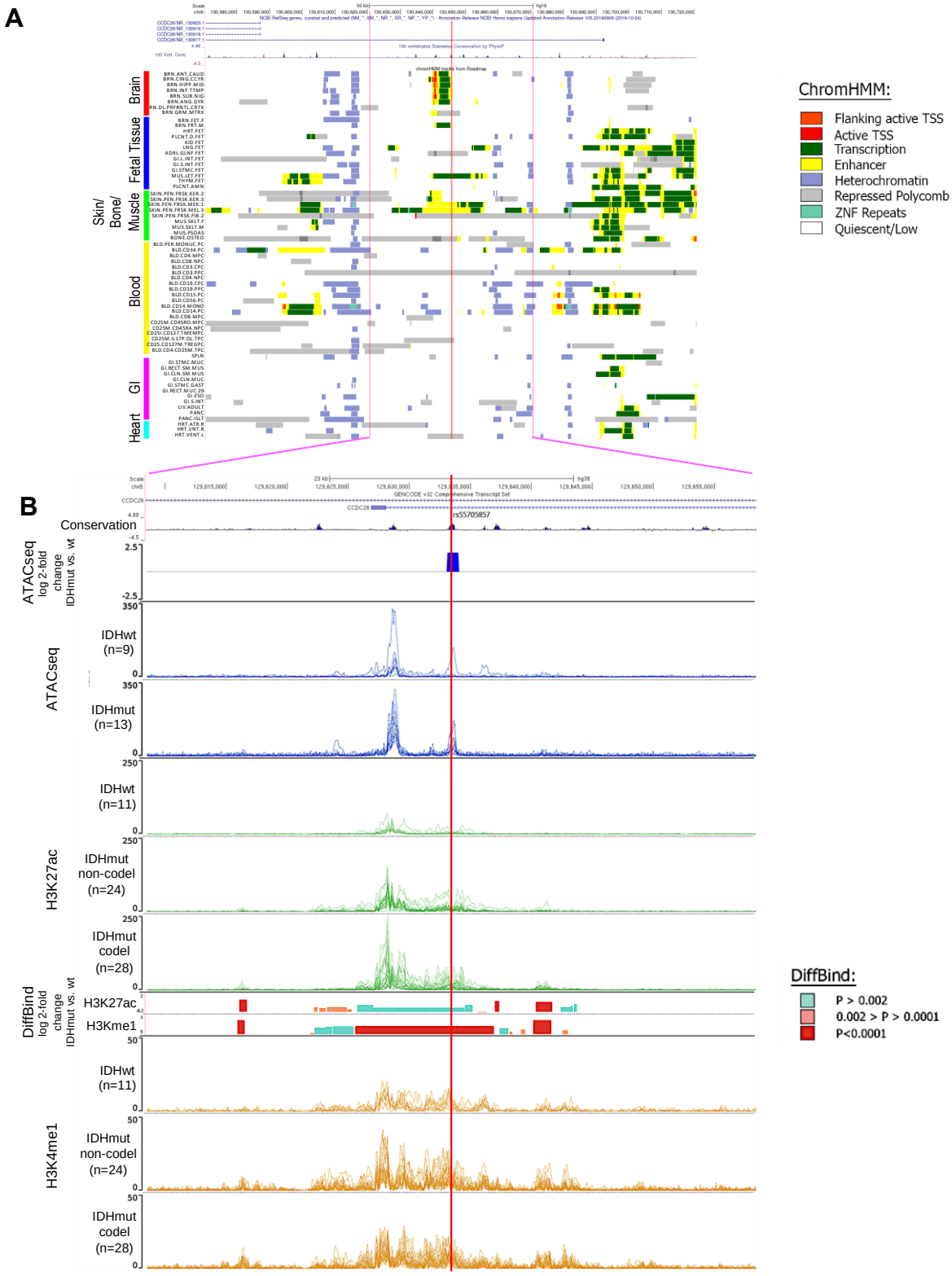

Fig. S1. rs55705857 is located in a brain-specific enhancer at 8q24

(**A**) Roadmap and ENCODE data showing the overlap between rs55705857 (indicated by the red line) and enhancer features in 64 normal tissues and normal blood, including the brain.

(**B**) Genomic locus surrounding rs55705857 (chr8:129,608,396-129,658,495; hg38). ATACseq data from the TCGA LGG and GBM, stratified by *IDH* mutation status, are displayed, each line represents an individual tumor (dark blue tracings). The fold change between the ATACseq signal for *IDH*-mutant vs. *IDH*-WT is displayed just above the tracings (blue, 0.001>p>0.002). ChIPseq signals for H3K27ac (dark green) and H3K4me^{1} (orange) are shown for the Mayo cohort of tumors, stratified into *IDH*-WT, *IDH*-mutant non-codel and *IDH*-mutant codel groups. DiffBind shows the fold change and p-value between the *IDH*-mutant vs. *IDH*-WT for both H3K27c and H3K4me^{1} (blue, 0.001>P>0.002; pink, 0.002>P>0.0001; red, P<0.0001). Red line indicates position of rs55705857.

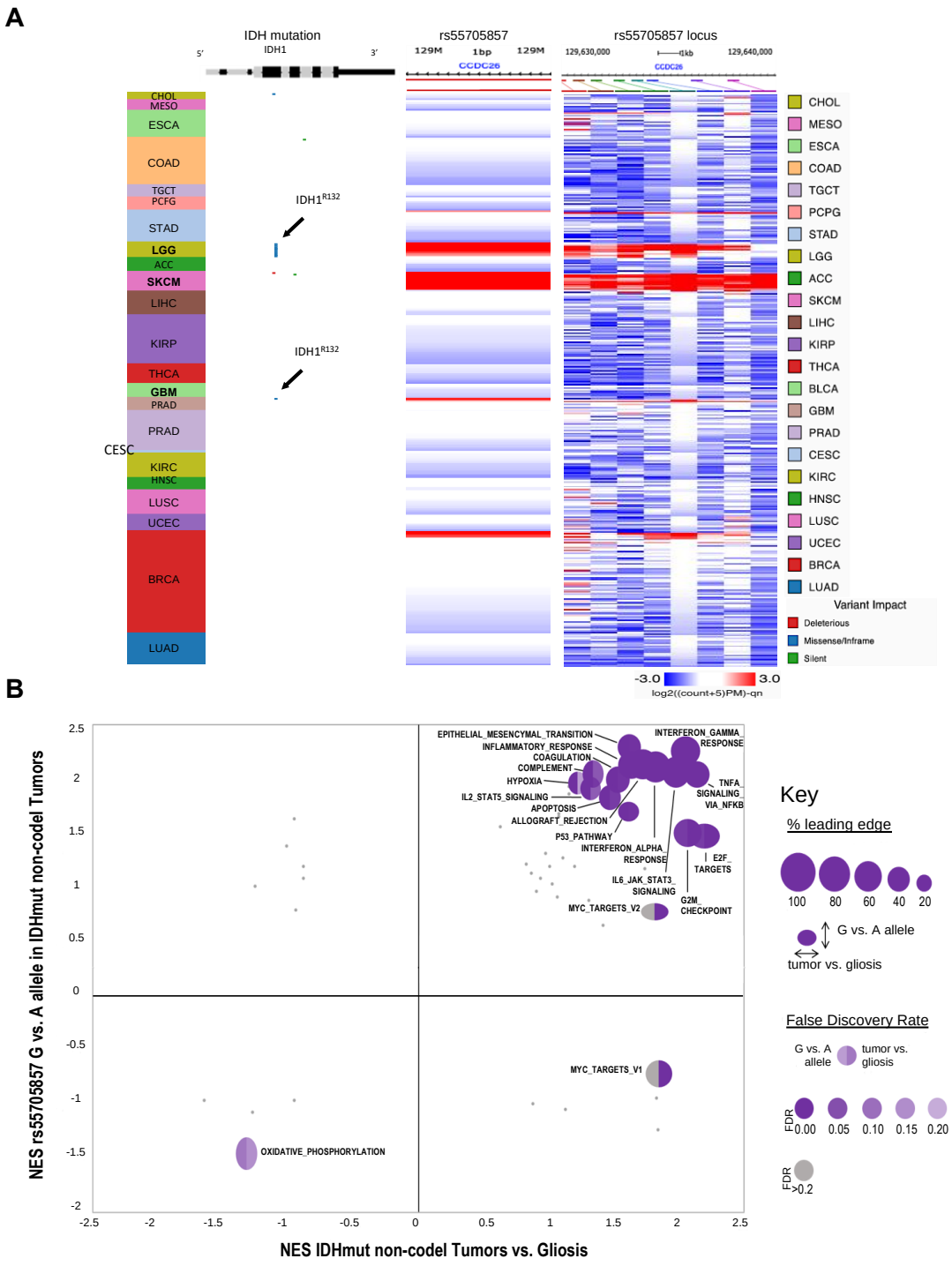

Fig. S2.

rs55705857 risk allele G enhances an LGG-transcriptional profile

(**A**) *IDH1* mutation and ATAC-seq accessibility at rs55705857 SNP (chr8:129,633,446; hg38) and at genomic locus surrounding rs55705857 (chr8:129,630,000-129,640,000) in 377 TCGA samples across 23 cancer types using UCSC Xena. (**B**) Comparison of GSEA results using 50 Hallmark gene sets in *IDH*-mutant non-codel tumors vs. gliosis and rs55705857 A vs. G allele in *IDH*-mutant non-codel tumors. Of note, the rs55705857-G risk allele is associated with upregulation of one MYC subset (Hallmark MYC Targets V2) but downregulation of another (Hallmark MYC Targets V1), but the FDRs for the MYC gene sets are 1.00 and 0.95 for MYC V1 and V2, respectively. The poor FDRs for this comparison prompted us to look at other MYC gene sets and to develop a glioma-specific MYC gene sets to see if the G allele is associated with a other MYC gene sets.

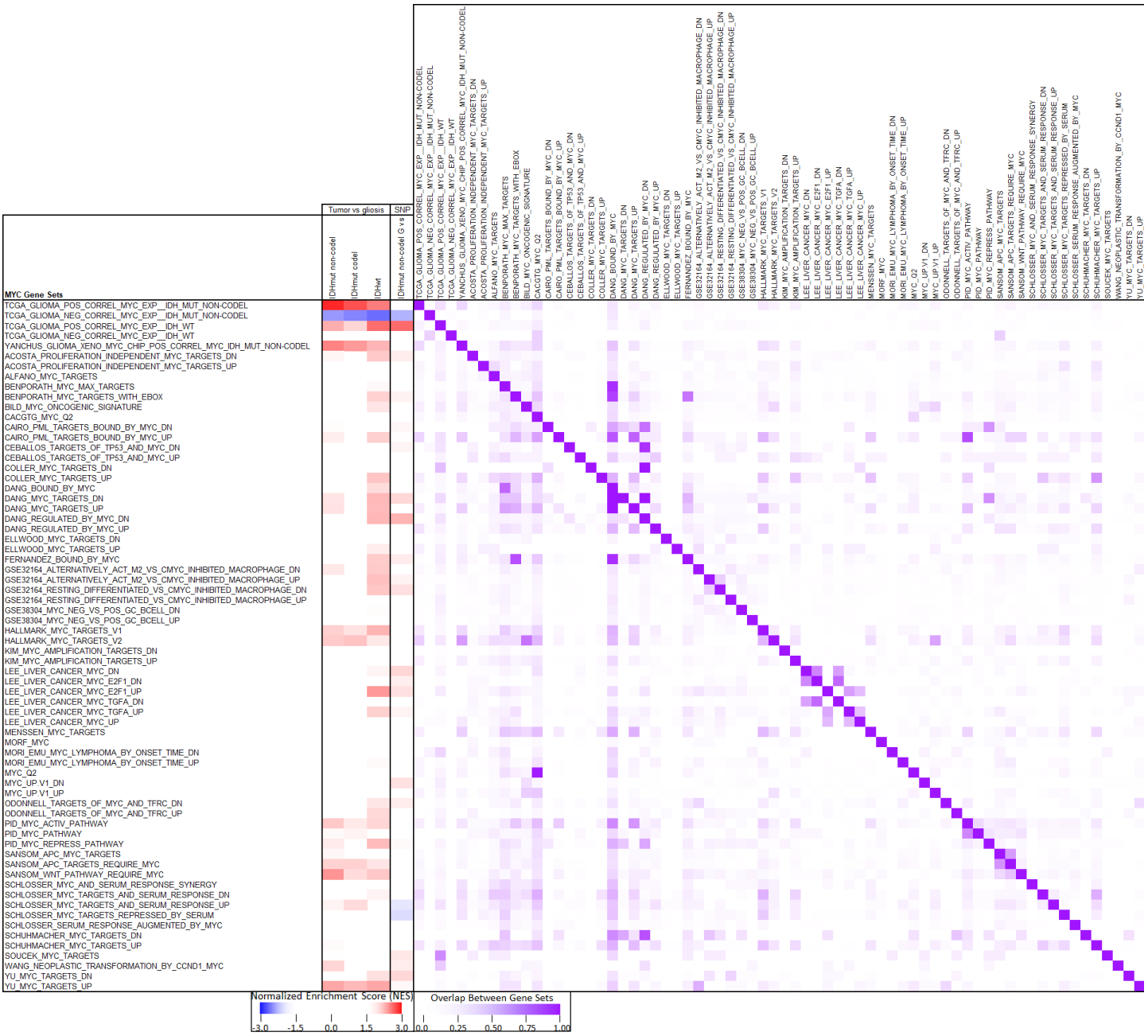

Fig. S3. MYC target gene signatures in IDH-mutant and IDH-*WT* glioma

Heatmap showing (1) normalized enrichment scores of the 50 Hallmark gene sets comparing *IDH*-mutant non-codel, *IDH*-mutant codel or *IDH*-WT tumors versus gliosis and rs55705857-G versus A allele in *IDH*-mutant non-codel tumors (left panel) and (2) the overlap between 63 different previously annotated MYC target gene signatures. Lower and the upper half of the heatmap shows the intersection of genes between 2 signatures as a percentage of genes in each of the two gene sets. Only gene sets with an FDR $q \leq 0.05$ in at least one comparison are included and colored in the heat map, the darker red and blues have an FDR $q < 0.001$.

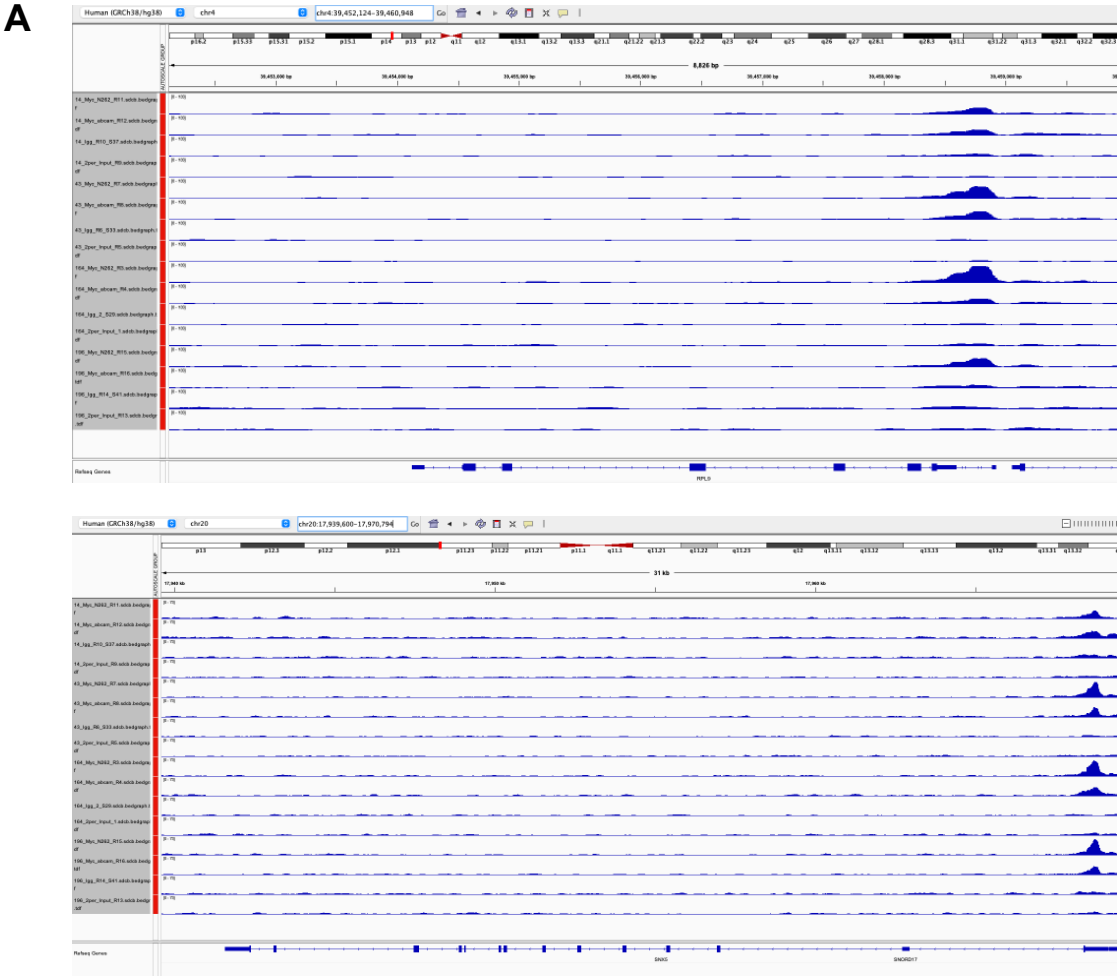

Fig. S4. MYC ChIPseq and GSEA

(**A**) Representative IGV tracks showing MYC ChIP reads using the N262 or the abcam ab32072 antibody as well as an IgG control as well as 2% input track.

(**B**) GSEA plot showing TCGA_GLIOMA_POS_CORREL_MYC_EXP_IDH_WT: glioma versus gliosis and rs55705857 G versus A tumor.

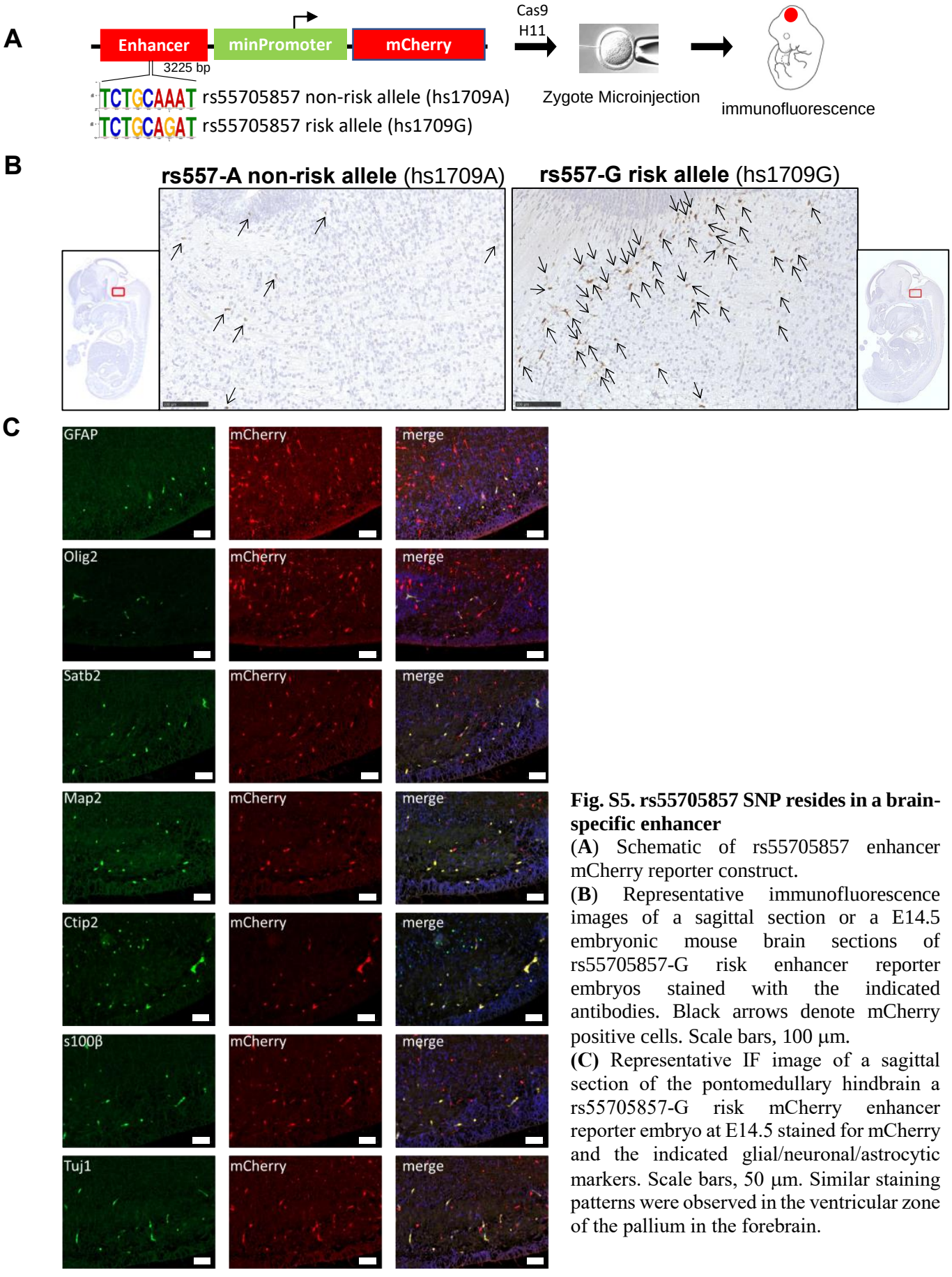

Fig. S5. rs55705857 SNP resides in a brain-specific enhancer

(**A**) Schematic of rs55705857 enhancer mCherry reporter construct.

(**B**) Representative immunofluorescence images of a sagittal section or a E14.5 embryonic mouse brain sections of rs55705857-G risk enhancer reporter embryos stained with the indicated antibodies. Black arrows denote mCherry positive cells. Scale bars, 100 μm.

(C) Representative IF image of a sagittal section of the pontomedullary hindbrain a rs55705857-G risk mCherry enhancer reporter embryo at E14.5 stained for mCherry and the indicated glial/neuronal/astrocytic markers. Scale bars, 50 μm. Similar staining patterns were observed in the ventricular zone of the pallium in the forebrain.

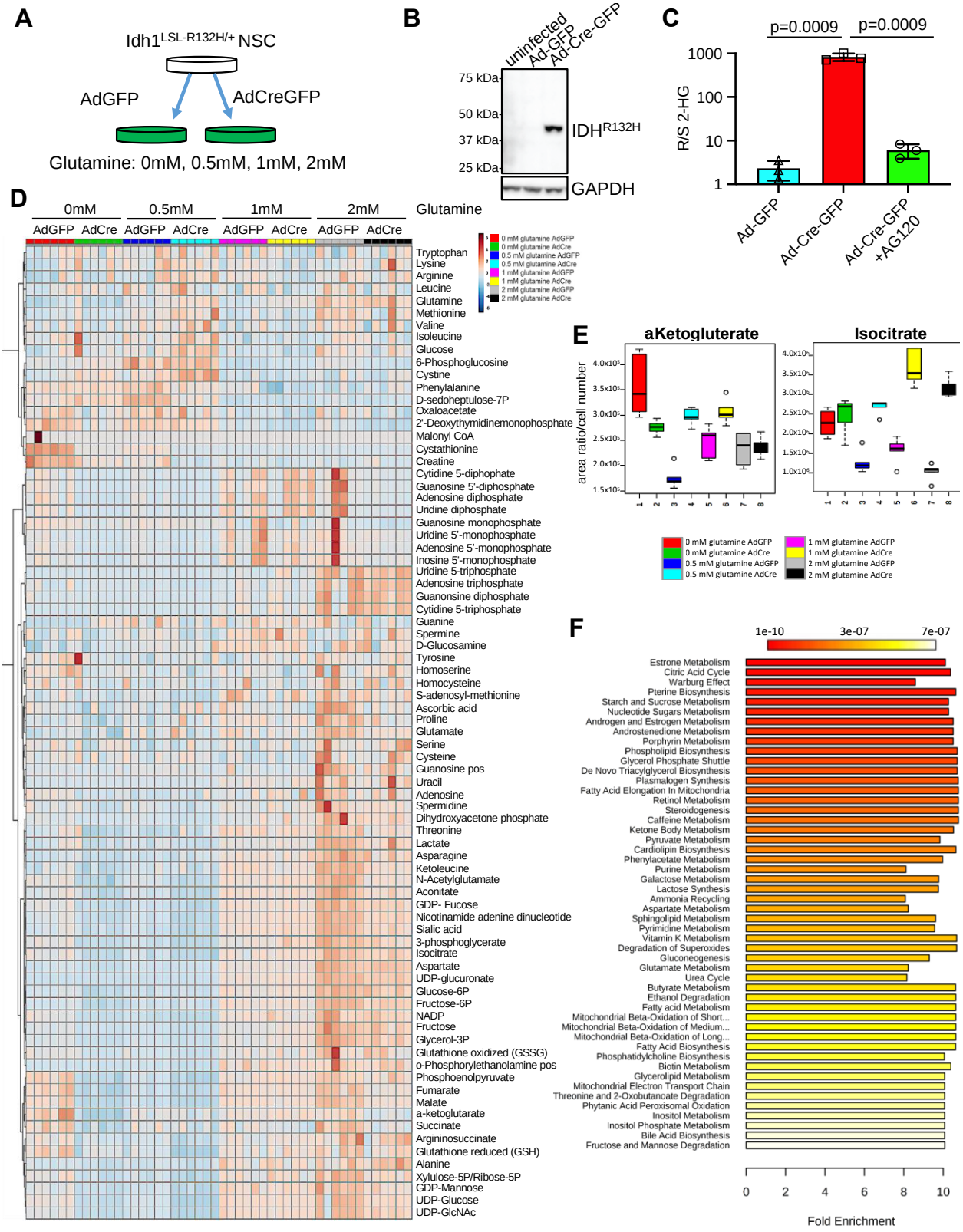

Fig. S6. IDH1^{R132H} metabolically rewires NSC

(**A**) Schematic of Idh^{R132H} induction in mouse NSC.

(B) Western blot of Idh1^{R132H} expression in uninfected or Ad-GFP or Ad-Cre-GFP transduced LSL-

Idh1^{R132H} mouse NSC using an IDH1^{R132H} specific antibody.
(**C**) Ratio of R- to S-2HG in LSL-*Idh1*^{R132H} mouse NSC transduced with Ad-GFP or Ad-Cre-GFP and treated with or without AG120 measured by mass spectrometry. Statistical comparison was performed using two-tailed t-test.
(**D**) Heatmap of 79 metabolites in syngeneic *Idh1*$^{+/+}$ and *Idh1*$^{R132H/+}$ NSC cultured in 4 different glutamine concentrations measured in sextuplicate by mass spectrometry.
(**E**) Normalized concentrations of isocitrate and the α-ketoglutarate in syngeneic *Idh1*$^{+/+}$ and *Idh1*$^{R132H/+}$ NSC cultured in 4 different glutamine concentrations measured in sextuplicate.
(**F**) Bar chart of enrichment analysis of metabolic pathways altered in syngeneic *Idh1*$^{R132H/+}$ compared to syngenic *Idh1*$^{+/+}$ NSC cultured in 4 different glutamine concentrations. Scale bar at the top indicates p-value.

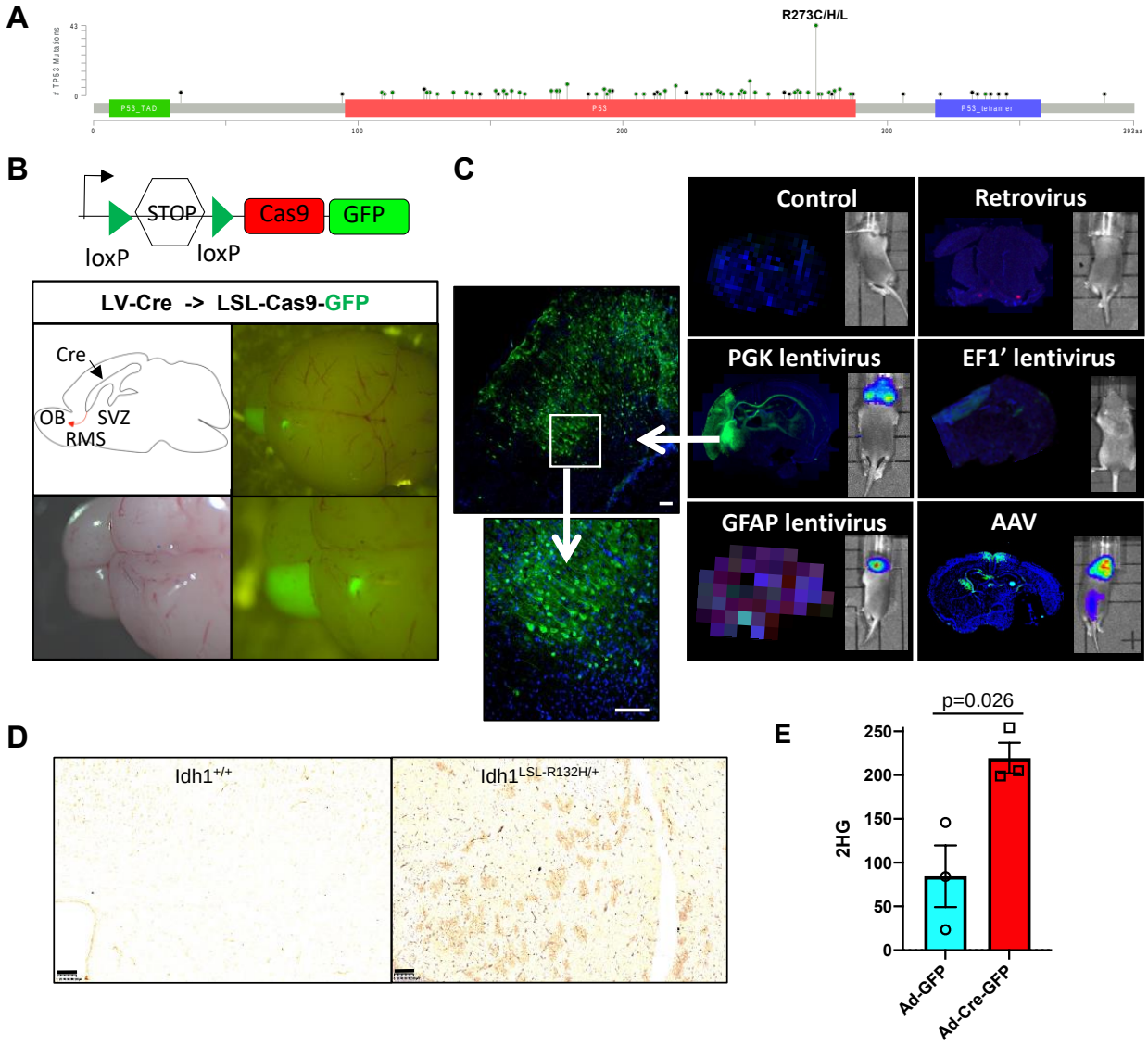

Fig. S7. *In vivo* Transduction of the Mouse Brain

(**A**) Lollipop plot depicting *TP53* mutations found in human LGG (data from the TCGA database).

(**B**) Schematic of the LSL-Cas9-GFP mouse cassette (Top). Schematic of the viral Cre injection targeting NSC of the SVZ of LSL-Cas9-GFP reporter mice, which leads to linage tracing of neural stem/progenitors and their progeny in the rostral migratory stream (RMS) and olfactory bulb (OB). Brightfield and fluorescent images of LSL-Cas9-GFP mouse brains at postnatal day 21 (P21) transduced with lentiviral Cre at P1.

(**C**) Representative immunofluorescent and bioluminescence images of LSL-Cas9-GFP brains at postnatal day 7 (P7) transduced with lentivirus (LV), adenovirus and adeno associated virus (AAV) expressing Cre at P1. Of all tested Cre-expressing viruses, LV-Cre showed the best labeling of the NSC in the SVZ and GFP-linage tracing of their progeny in the midbrain. Scale bars, 50 μm.

(**D**) Representative histological IHC images using an IDH1^{R132H}-specific antibody of an *Idh1*$^{+/+}$ (left) and *Idh1*$^{LSL\text{-}R132H/+}$ (right) brain transduced with LV- Cre. Scale bar, 100 μm.

(**E**) 2HG levels in LSL-*Idh1*^{R132H} mouse brains transduced with Ad-GFP and Ad-Cre-GFP. Statistical comparison was performed using two-tailed t-test.

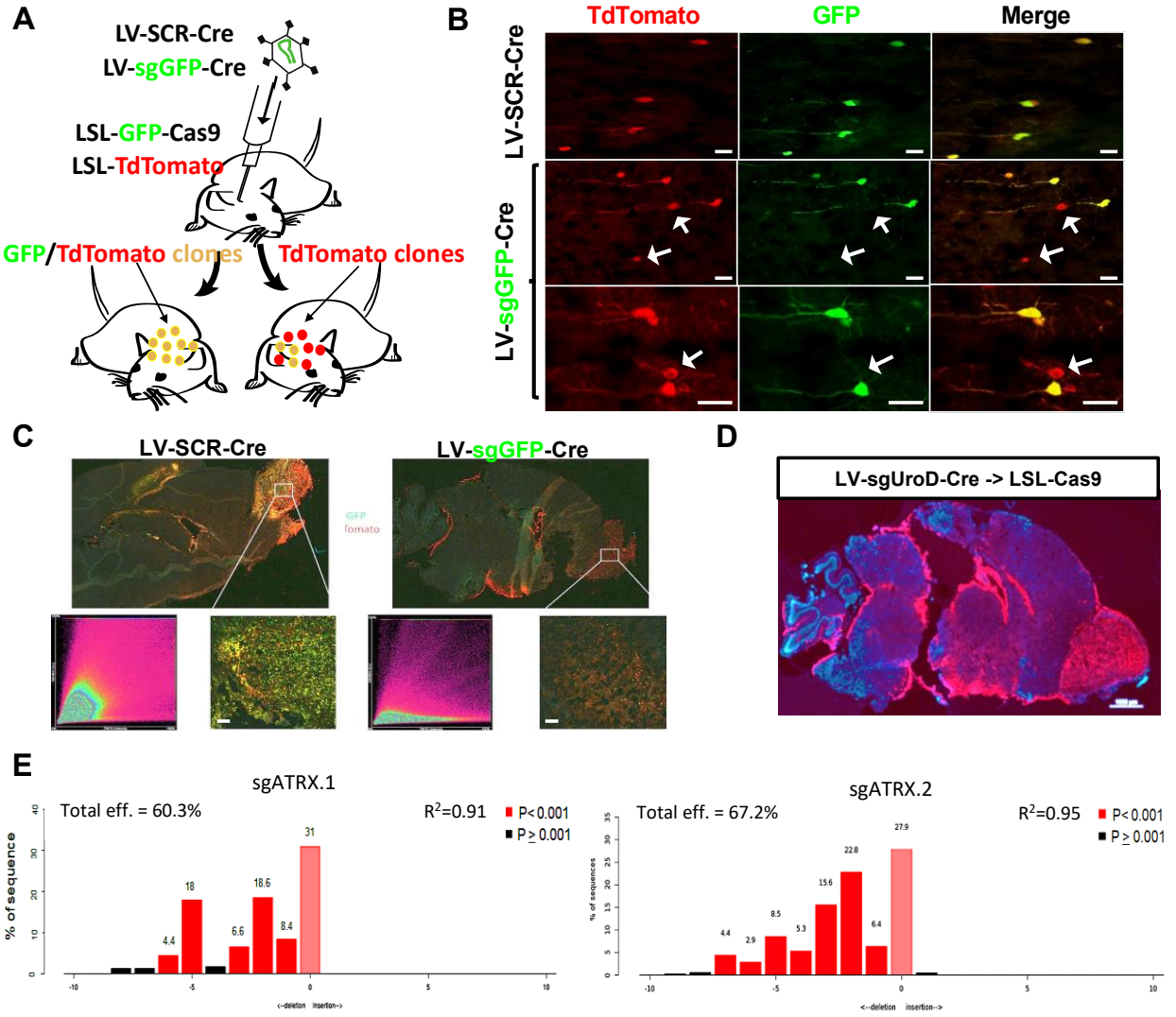

Fig. S8. *In vivo* CRISPR methodology in the Mouse Brain

(**A**) Schematic depicting our *in vivo* double fluorescent reporter strategy to quantify efficacy of CRIPSR/Cas9-mutagenesis. LSL-Cas9-GFP; LSL-tdTomato mice transduced with LV-Cre encoding a scrambled sgRNA (LV-Scr-Cre) co-express green fluorescent protein (GFP) and tdTomato. Mice transduced with LV-Cre targeting GFP (LV-sgGFP-Cre) exhibit tdTomato^{+} cells lacking GFP, allowing for quantification of GFP knockout efficacy by IF and/or FACS, revealing a knock-out efficiency of 85±5%.

(**B**) Representative fluorescent images of tdTomato and GFP expression within brains of LSL-Cas9-GFP TdTomato mice transduced with LV-Cre carrying either sgScr (top) or sgGFP (middle, bottom). White arrows indicate loss of GFP expression in tdTomato positive cells. Scale bar, 25 μm.

(**C**) Expression of GFP and tdTomato in brains of LSL-Cas9-GFP; LSL-tdTomato mice transduced with LV-Cre constructs expressing either sgScr (top left) or sgGFP (top right). Co-localization analysis plot depicting GFP and RFP intensities on the Y- and x-axis, respectively (bottom left) and 10x magnification of respective images (bottom right). Scale bar, 50 μm.

(**D**) Fluorescent image of a sagittal section of whole LSL-Cas9-GFP brain transduced with LV-sg*Urod*-Cre. To confirm efficient mutagenesis of an endogenous gene, we targeted the heme biosynthesis gene *Urod*. Loss of *Urod* leads to accumulation of unprocessed, fluorescent porphyrins (*73*) and bright red fluorescence in the SVZ, the cerebrum and olfactory bulb (OB)

(**E**) Bar graph showing spectrum of indels and their frequencies for two sgRNAs targeting *Atrx* using Tracking of Indels by Decomposition algorithm (TIDE).

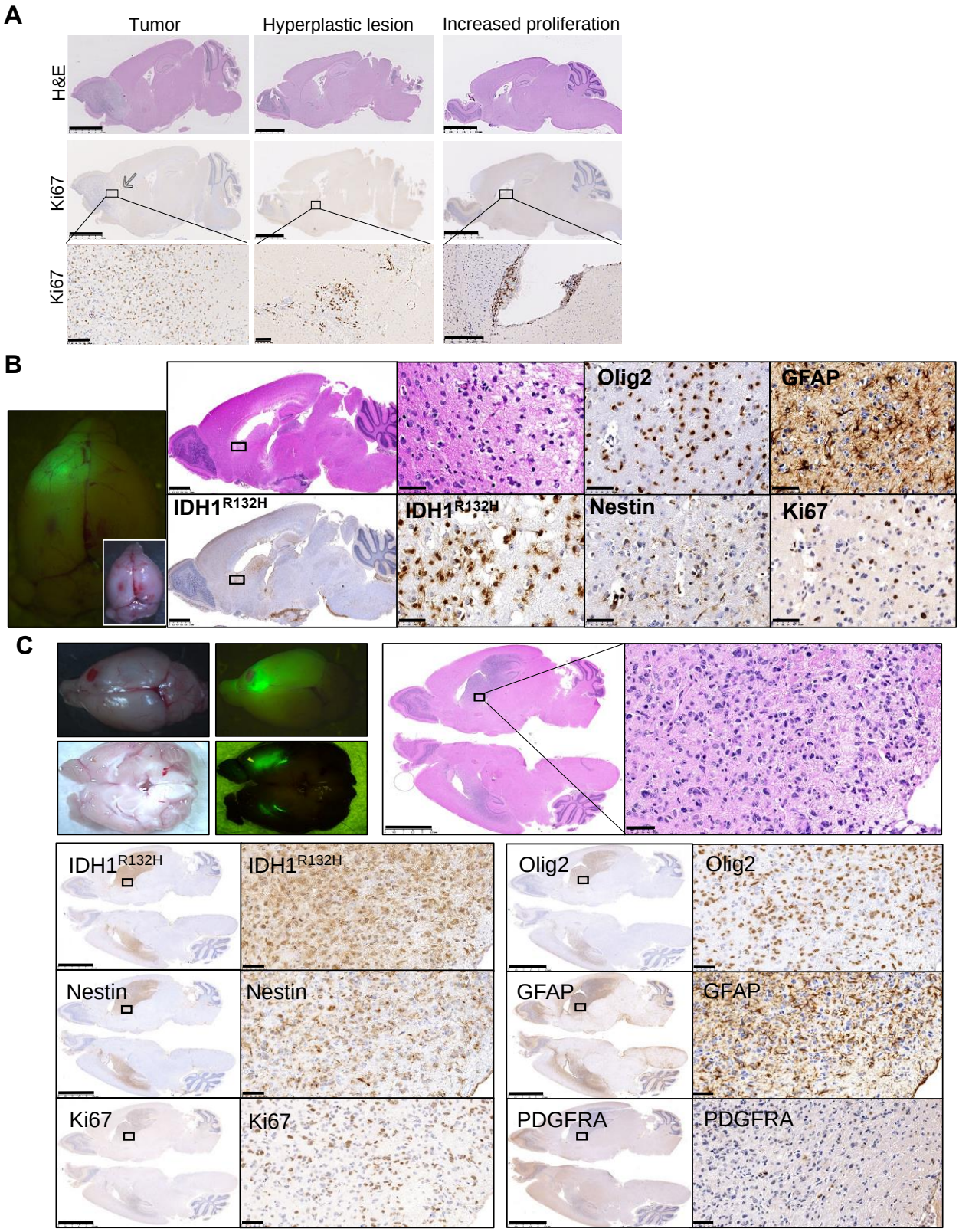
A
Tumor
Hyperplastic lesion
Increased proliferation
H&E
Ki67
Ki67
B
Olig2
GFAP
IDH1R132H
IDH1R132H
Nestin
Ki67
C
IDH1R132H
IDH1R132H
Olig2
Olig2
Nestin
Nestin
GFAP
GFAP
Ki67
Ki67
PDGFRA
PDGFRA

Fig. S9. Mouse model of LGG histologically recapitulates human tumors

(A) Representative H&E and Ki67 staining of a tumor, a hyperplastic lesion and a lesion with increased proliferation in the subventricular zone (SVZ) illustrating the classification scheme used to determine cohort phenotypes in Fig. 3C and 4B. Scale bars, 2.5 mm (top and middle) and 100μm (bottom).**(B**) Representative brightfield and fluorescent image of mouse LGG brain (left) as well as H&E and IHC staining of the same tumor region within a sg*Atrx; Idh1*$^{R132H/+}$; *Trp53*$^{R270H/+}$; Cas9-GFP brain using the indicated antibodies. Scale bars, 2.5 mm (left) and 50 μm (right). (**C**) Representative brightfield and fluorescent image of mouse LGG brain (top left) as well as H&E staining (top right), and immunohistochemical staining of the same tumor region within a sg*Atrx; Idh1*$^{R132H/+}$;*Trp53*$^{R270H/fl}$; Cas9-GFP brain using the indicated antibodies (bottom). Scale bars, 2.5 mm and 50 μm for close-ups.

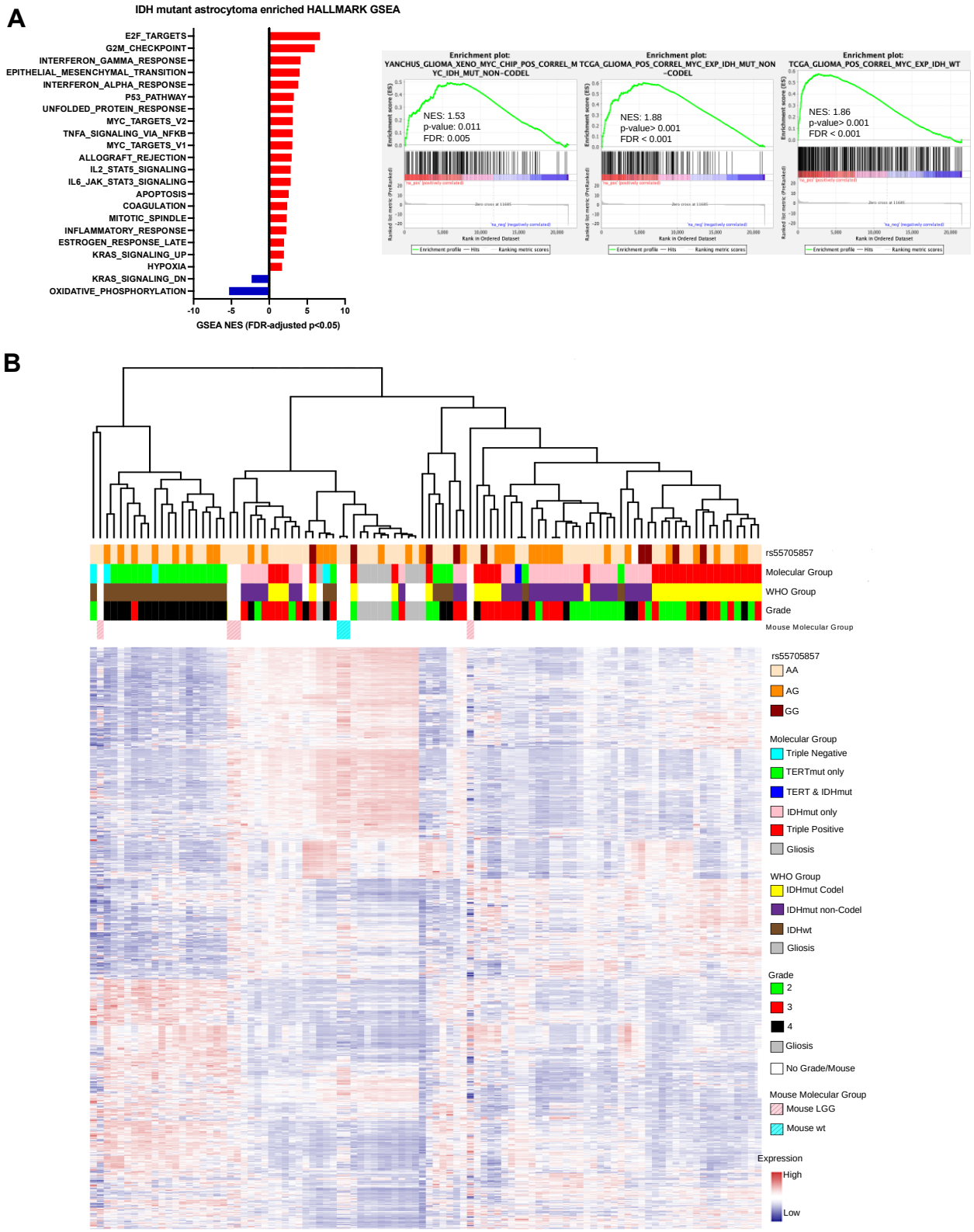

Fig. S10. Mouse model of LGG molecularly recapitulates human tumors

(**A**) Comparison of GSEA analysis of 50 Hallmark gene sets in mouse LGG vs. mouse brain. Bar graph shows the top differential pathways ranked by NES with nominal p-value <0.05 and GSEA plots show selected pathways.

(**B**) Unsupervised hierarchical clustering of RNA expression of mouse sg*Atrx*; *Idh1*$^{R132H/+}$; *Trp53*$^{R270H/+}$; Cas9-GFP brain tumors, human LGG and human gliosis.

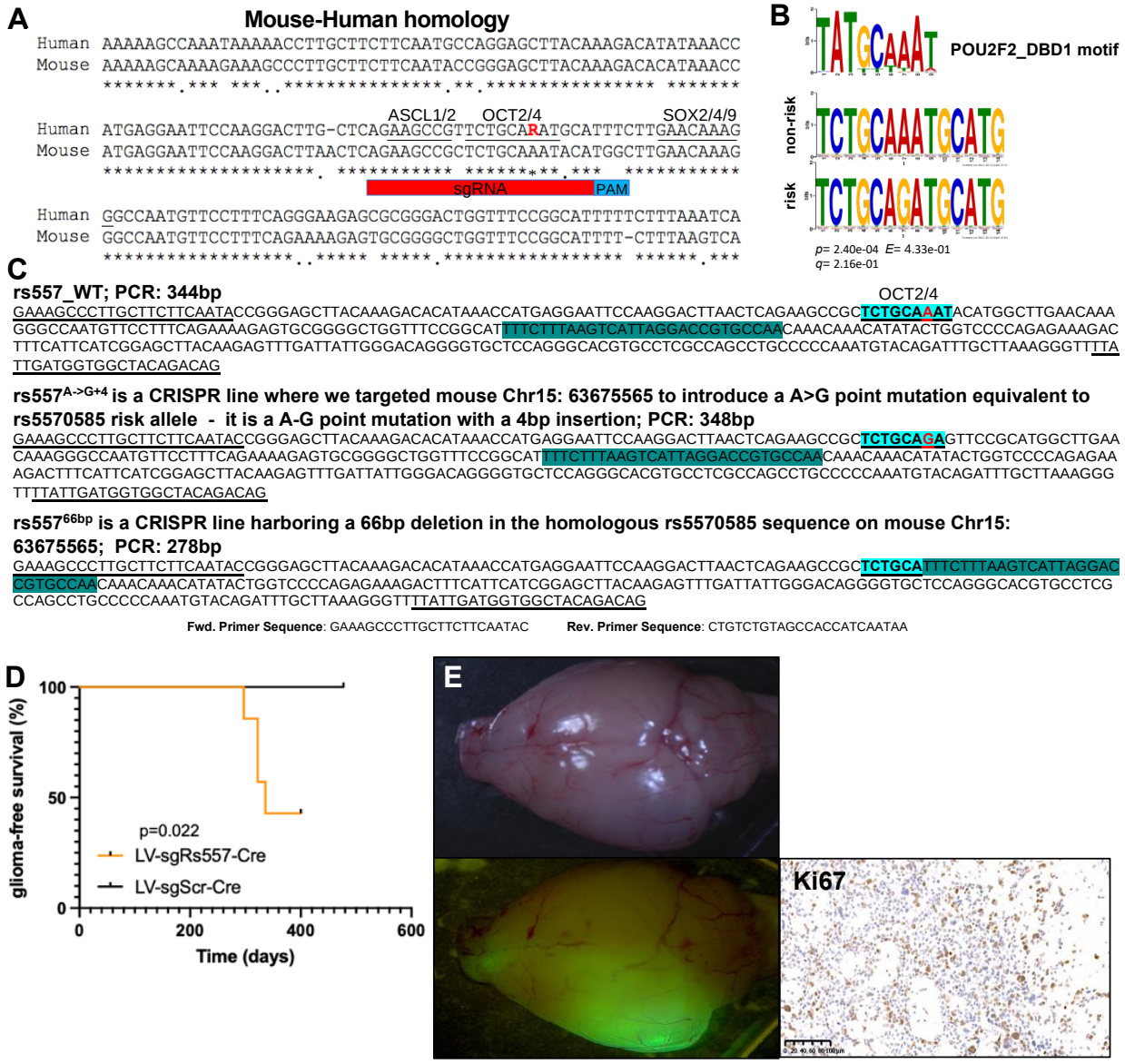

Fig. S11. Generation of rs55705857-mimetic mice

(**A**) Sequence alignment of human rs55705857 region on chromosome 8q.24.21 with the syntenic region on mouse chromosome 15.

(**B**) OCT2 (POU2F2) motif (top) aligned with the rs55705857 non-risk (middle) and risk (bottom) allele.

(**C**) Sanger sequencing results of the PCR amplicon encompassing the syntenic mouse rs55705857 region in wildtype and CRSIPR/Cas9-edited rs557$^{A->G+4}$ and rs557^{66bp} mouse strains.

(**D**) Survival of *Idh1*$^{R132H/+}$;*Trp53*$^{fl/fl}$; *Atrx*$^{fl/fl}$; Cas9-GFP mice transduced with an sgRNA targeting *rs557* or a scrambled control sgRNA (Scr). (p-value < 0.0001, Log-rank (Mantel-Cox) test)

(**E**) Representative whole brain fluorescent image and IHC for Ki67 of a brain injected with rs557$^{66bp/+}$,*Idh1*$^{R132H/+}$;*Trp53*$^{\Delta/\Delta}$;Cas9-GFP RIP cells. Scale bars, 100 μm

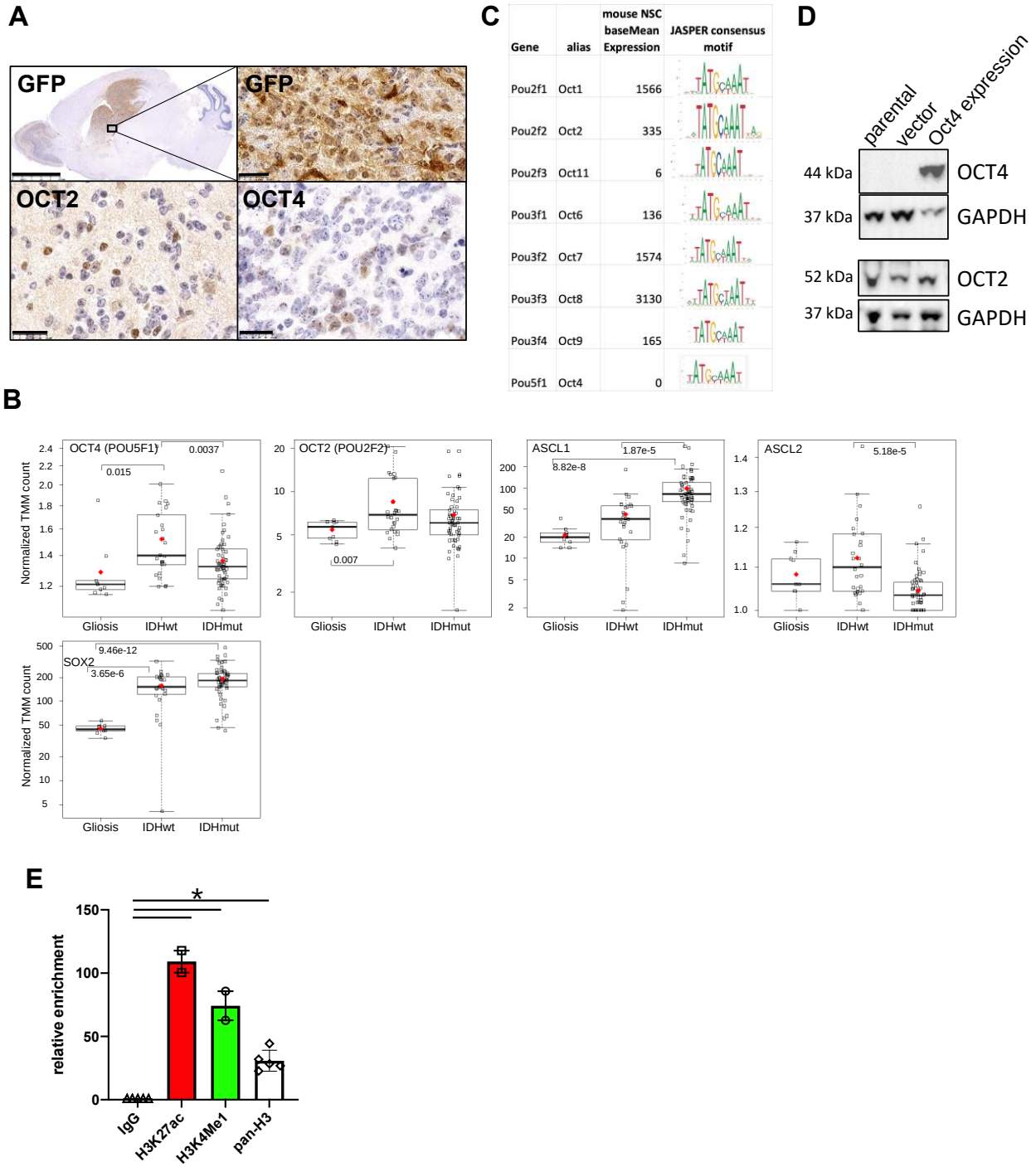

Fig. S12. The mouse orthologous rs55705857 locus is decorated with enhancer marks

(**A**) Representative IHC staining of Oct2 and Oct4 expression within rs557$^{66bp/+}$, *Idh1*$^{R132H/+}$; *Trp53*$^{fl/fl}$; Cas9-GFP mouse LGG. Scale bars, 25 μm.

(**B**) Expression levels for *OCT4* (*POU5F1*), *OCT2* (*POU2F2*), *ASCL1*, *ASCL2* and *SOX2* from patient glioma and gliosis samples measured by RNAseq. Tumors are stratified by *IDH* mutation, significant differences are shown with their p-values. Non-significant p-values are not shown.

(**C**) Expression levels and JASPAR consensus motif for all 8 Oct/Pou transcription factor family members measured by RNAseq in primary mouse NSC cultures.

(**D**) Western blot analysis of Oct2 and Oct4 in cultured RIP cells. GAPDH serves as loading control.

(**E**) Enrichment of H3K27Ac, H3K4me^1 and pan-H3 at mouse rs55705857 locus as determined by ChIP-qPCR using rs557$^{66bp/+}$, *Idh1*$^{R132H/+}$; *Trp53*$^{\Delta/\Delta}$-mutant RIP tumor cells (n = 3). IgG-IP serves as a negative control. Statistical comparison was performed using two-tailed t-test.

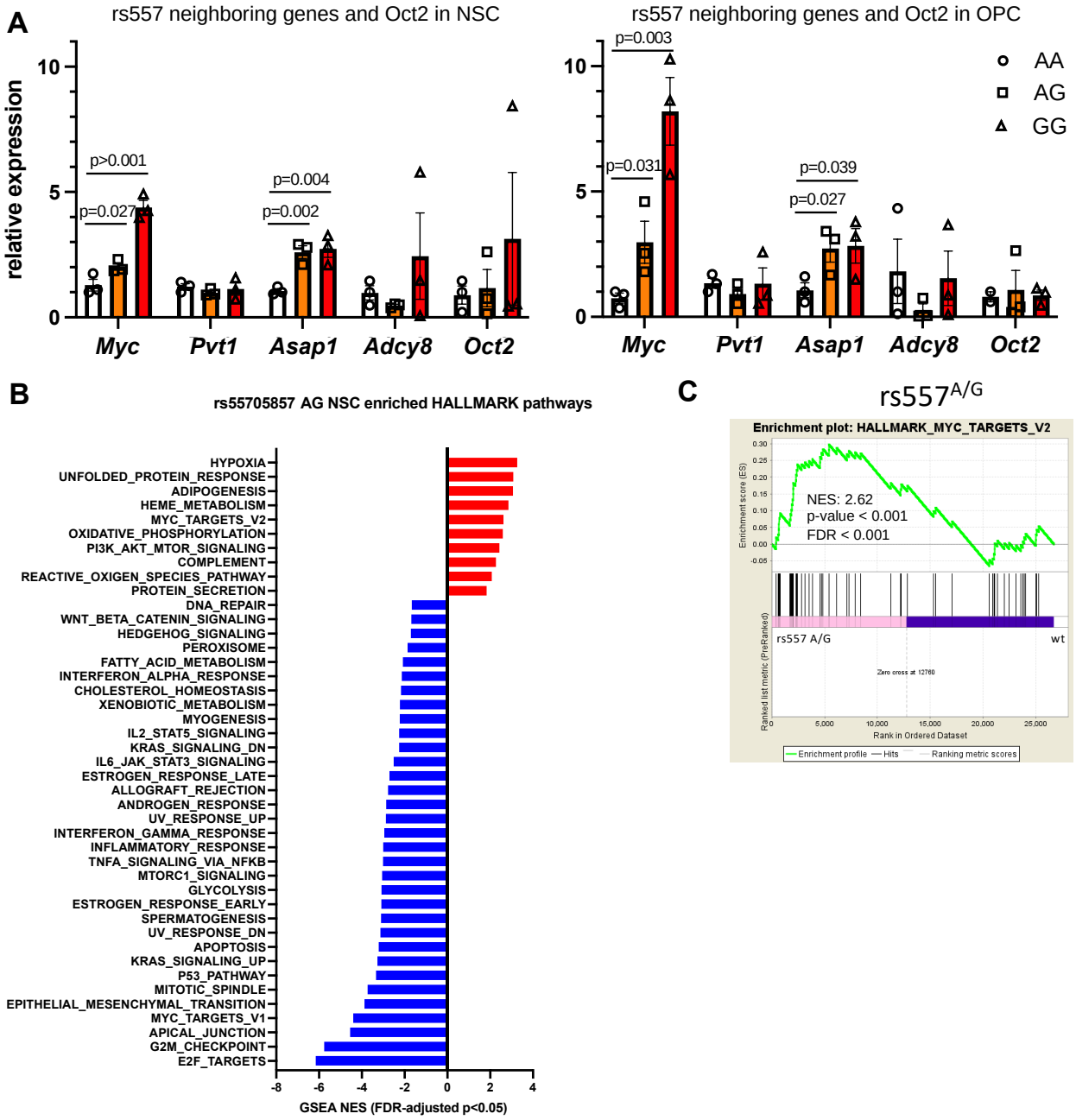

Fig. S13. rs55705857 regulates neighboring genes and alters transcriptional profile of NSCs

(**A**) Expression of the indicated rs55705857 neighboring genes and Oct2 measured by real-time qPCR in primary NSCs and NSC-derived OPC cultures isolated from homozygous rs557$^{G/G}$, heterozygous rs557$^{A/G}$ as well as wildtype rs557$^{A/A}$ littermate mice.

(**B**) Comparison of GSEA analysis of 50 Hallmark gene sets in primary mouse rs557$^{G/G}$, rs557$^{A/G}$ as well as wildtype rs557$^{A/A}$ NSCs. Bar graph shows the top differential pathways ranked by NES with nominal p-value <0.05.

(C) GSEA plot showing HALLMARK_MYC_TARGETS_V2 gene set distribution in rs557A$^{/G}$ versus wildtype rs557$^{A/A}$ NSCs.

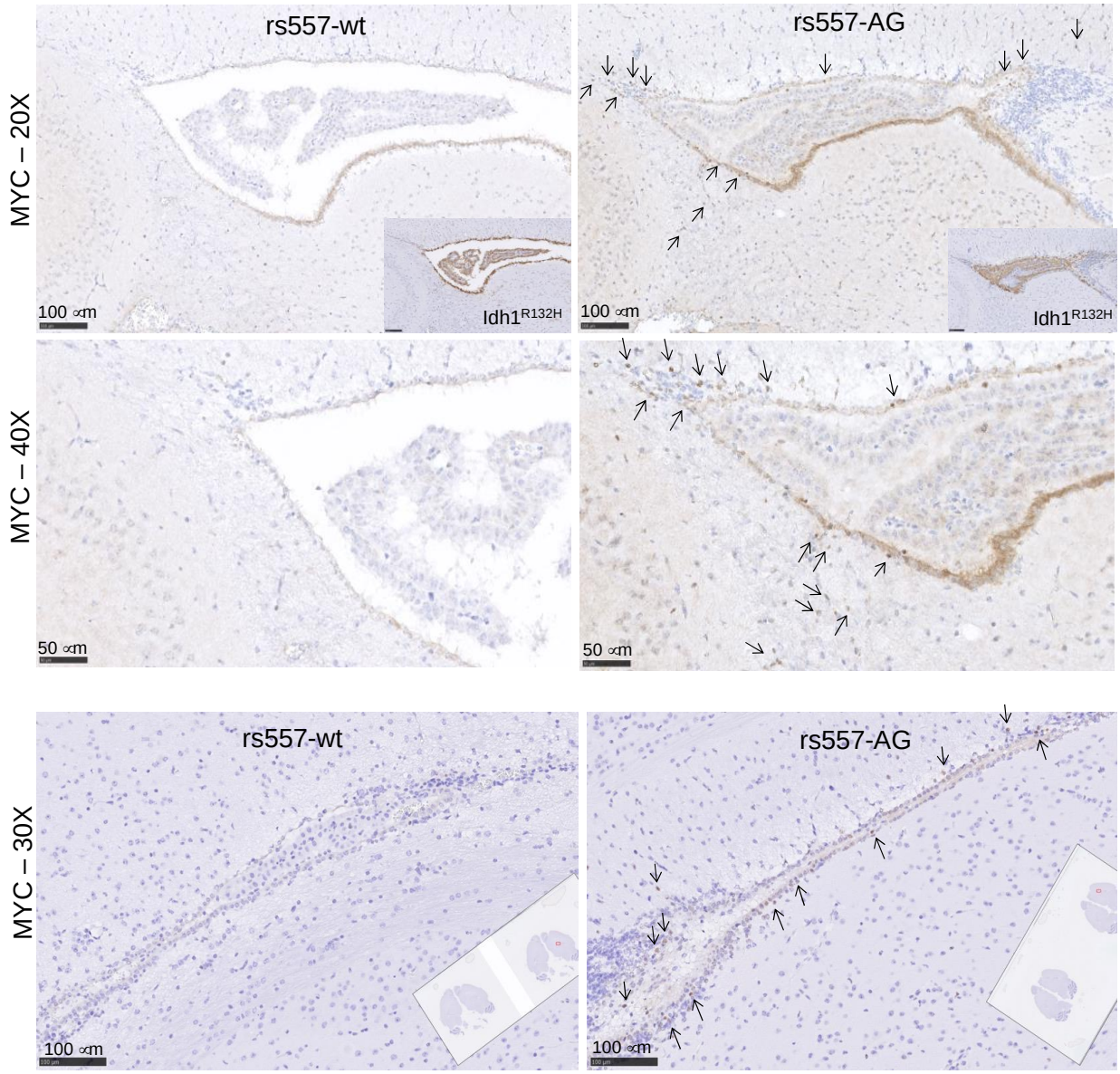

Fig. S14. Increased MYC expression in SVZ of rs55705857 mutant mice
Representative Myc IHC images in the subventricular zone (SVZ) of brains from heterozygous rs557$^{A/G}$ as well as wildtype rs557$^{A/A}$ littermate mice. Scale bars as indicated.

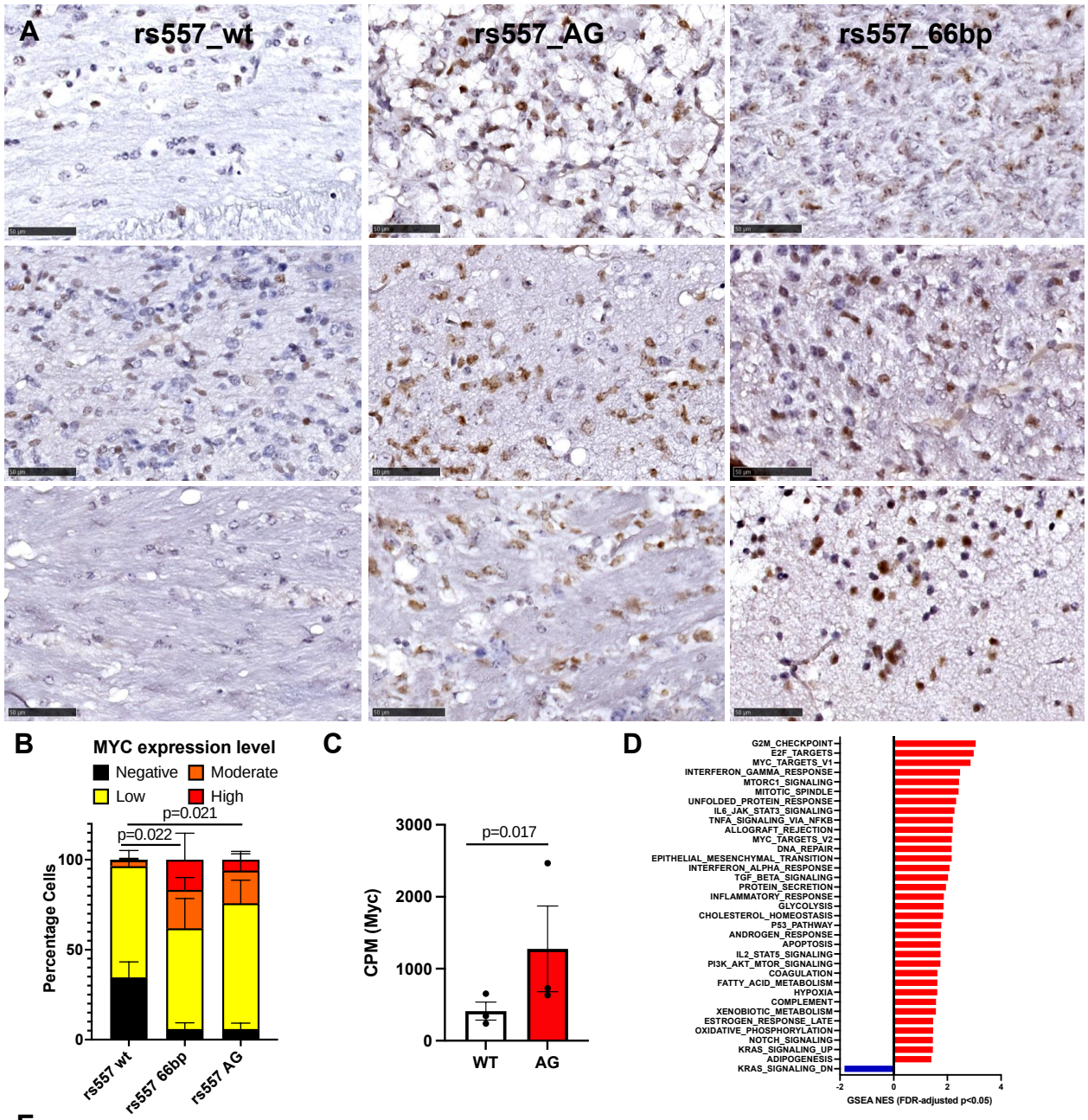

Fig. S15. Increased MYC expression in brain tumors of rs55705857 mutant mice

(**A**) Representative Myc IHC images of *Idh1*^{R132H}/*p53*/*Atrx*-mutant brain tumors from wildtype rs557$^{A/A}$, heterozygous rs557$^{A/G}$ as well as heterozygous rs557^{66bp} mice. Scale bars, 50 µm.

(**B**) Stacked bar graph depicting quantification of Myc staining in *Idh1*^{R132H}/*p53*/*Atrx*-mutant brain tumors from wildtype rs557$^{A/A}$, heterozygous rs557$^{A/G}$ as well as heterozygous rs557^{66bp} mice.

(**C**) Expression of Myc mRNA in *Idh1*^{R132H}*/p53/Atrx*-mutant brain tumors from wildtype rs557$^{A/A}$ and heterozygous rs557$^{A/G}$ mice.
(**D**) Comparison of GSEA analysis of 50 Hallmark gene sets in primary mouse rs557$^{G/G}$, rs557$^{A/G}$ as well as wildtype rs557$^{A/A}$ NSCs. Bar graph shows the top differential pathways ranked by NES with nominal p-value <0.05.
(**E**) GSEA plot showing HALLMARK_MYC_TARGETS_V1 and V2 gene set distributions in rs557$^{A/G}$ versus wildtype rs557$^{A/A}$ *Idh1*^{R132H}*/p53/Atrx*-mutant brain tumors.

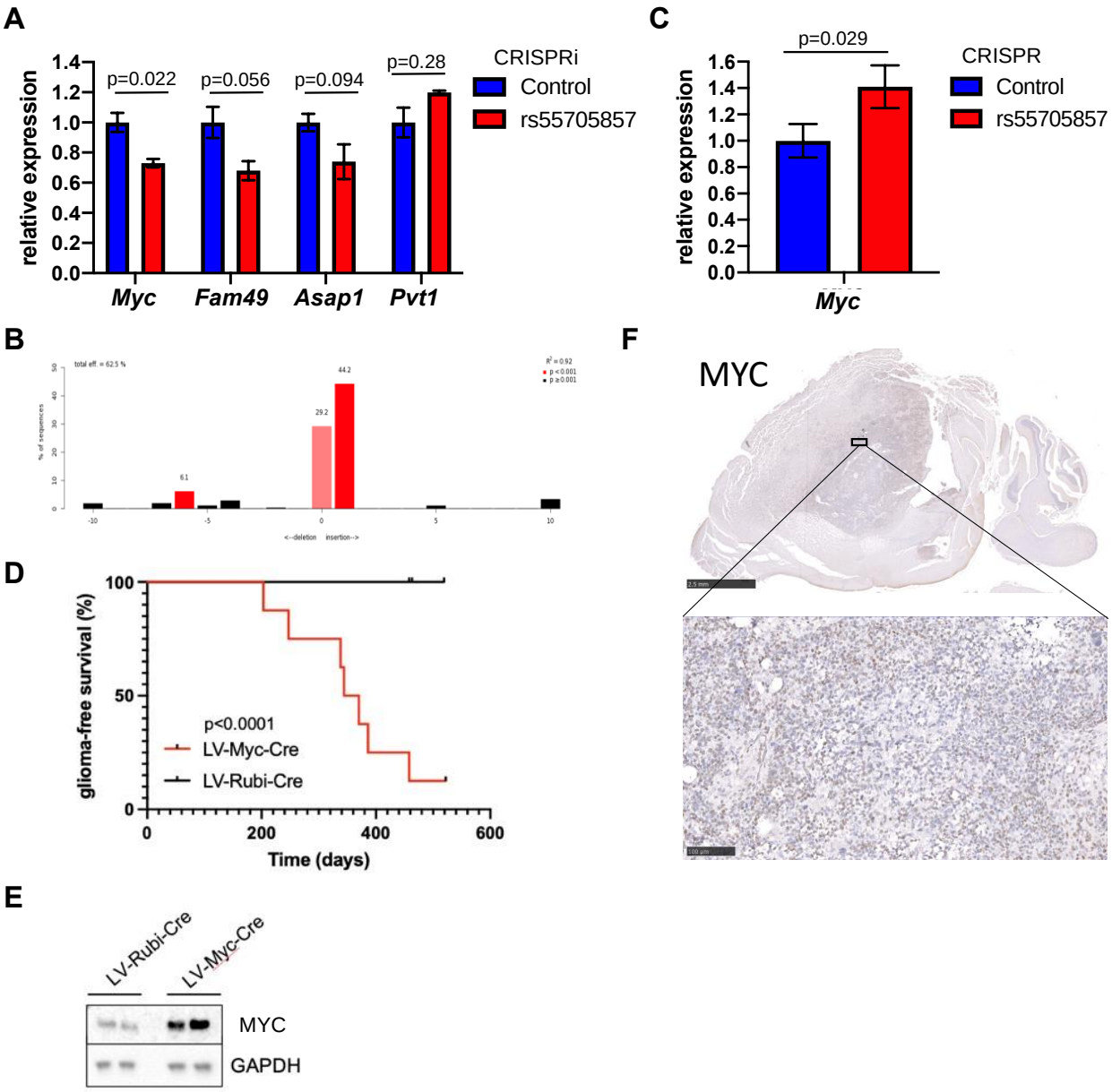

Fig. S16. rs55705857 regulates MYC expression

(**A**) Expression of rs55705857 neighboring genes measured by real-time qPCR without or with silencing the rs55705857 locus using CRISPRi. (p-value by two-tailed t-test).

(**B**) Bar graph showing spectrum of indels and their frequencies for a sgRNA targeting the WT rs55705857 allele in rs557$^{66bp/+}$ RIP cells using Tracking of indels by Decomposition algorithm (TIDE).

(**C**) Relative expression of *Myc* measured by real-time qRT-PCR in rs557$^{66bp/+}$ versus rs557-double mutant RIP cells. (p-value by two-tailed t-test).

(D) Survival of *Idh1*$^{R132H/+}$*;Trp53*$^{fl/fl}$; *Atrx*$^{fl/fl}$; Cas9-GFP mice with brain-specific transduction of an lentivirus expressing Cre and *Myc* or Cre and Rubi as a control. (p-value < 0.0001, Log-rank (Mantel-Cox) test)

(**E**) Western blot analysis of MYC protein in tumors from *Idh1*$^{R132H/+}$*;Trp53*$^{fl/fl}$; *Atrx*$^{fl/fl}$; Cas9-GFP mice transduced with an lentivirus expressing Cre and *Myc* or Cre and Rubi as a control.

(**F**) Representative MYC-IHC image of a brain from a *Idh1*$^{R132H/+}$*;Trp53*$^{fl/fl}$; *Atrx*$^{fl/fl}$; Cas9-GFP mouse transduced with an lentivirus expressing Cre and *Myc*. Scale bars, 2.5 mm upper panel and 100 μm lower panel.

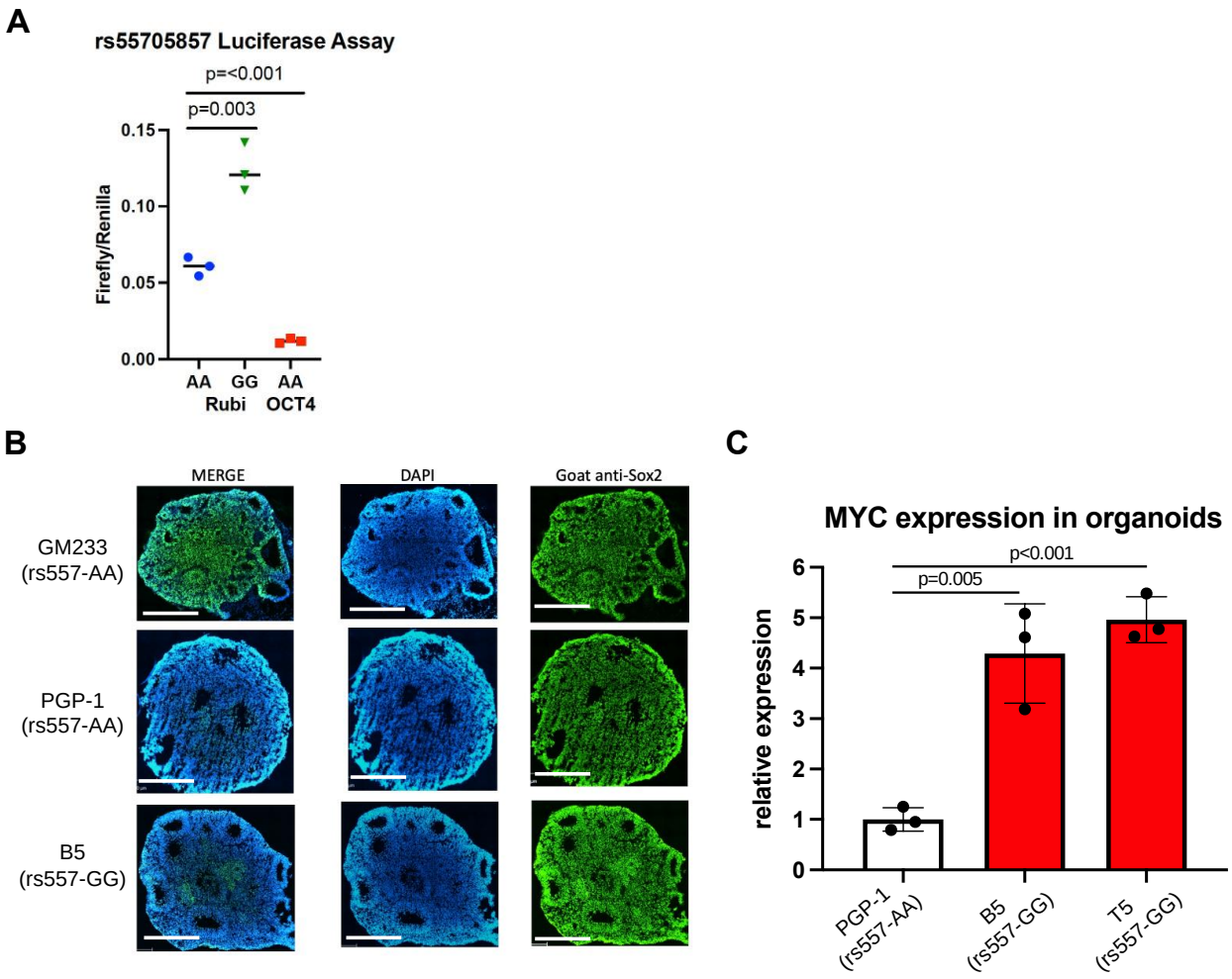

Fig. S17. rs55705857 regulates MYC in human cells and Cerebral Organoids
(**A**) MYC luciferase reporter assay showing increased transactivation of the rs55705857-G risk allele compared to the rs55705857-A non-risk allele and that overexpression of OCT4 reduces transactivation of the rs55705857-A allele compared to mRubi control vector.
(**B**) Representative images of 4 week-old cerebral organoids derived from human iPSC cell lines PGP1 and GM233 or the isogenic PGP1-derived CRISPR-edited rs55705857-G/G clones B5. Scale bars, 1 mm.
(**C**) Relative expression of *Myc* mRNA levels measured by real-time qRT-PCR in cerebral organoids established from human PGP1 iPSCs or the indicated isogenic PGP1-derived CRISPR-edited rs55705857-G/G clones. (p-value by two-tailed t-test).

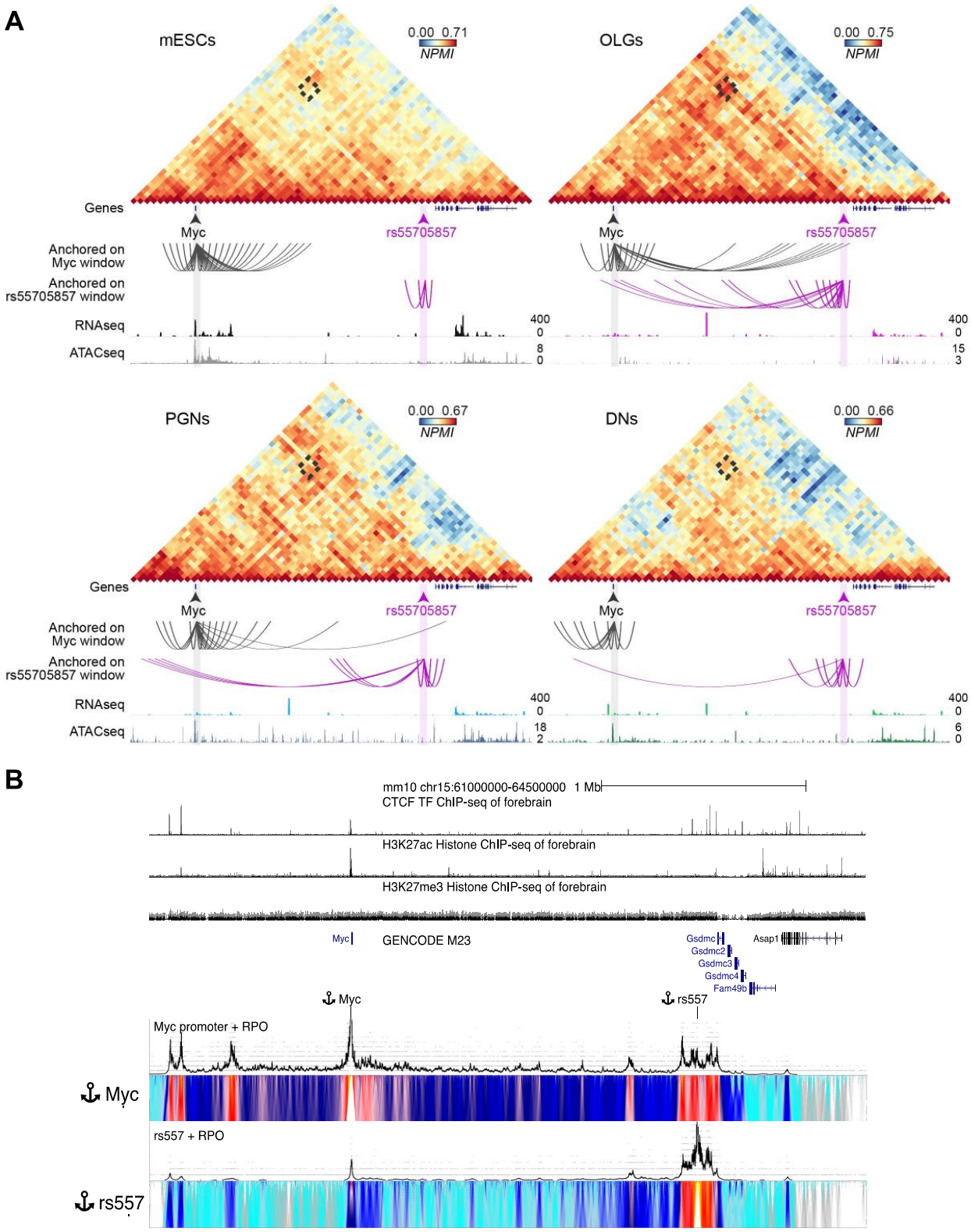

Fig. S18. rs55705857 interacts with MYC

(**A**) Genome Architecture Mapping (GAM) contact matrix of the genomic window chr15:61,500,000-64,500,000 showing strong interaction between MYC and the rs55705857 locus in mouse oligodendrocytes and their precursors (OLGs) in the somatosensory cortex but lack of such an interaction in mouse embryonic stem cells (mESCs), terminally differentiated pyramidal glutamatergic neurons (PGNs) from the cornu

ammonis 1 (CA1) of the dorsal hippocampus, and dopaminergic neurons (DNs) from the ventral tegmental area (VTA) of the midbrain. Spider plots were used to show strong GAM interactions for the indicated single genomic window of interest (MYC and rs55705857), which were determined as the 85th percentile NPMI cutoff for each cell type. RNAseq and ATACseq tracks represent normalized pseudobulk reads from scRNA-seq and scATAC-seq, respectively, except for bulk ATAC-seq from mES cells.
(**B**) Analysis of high frequency interacting regions at the *Myc* locus in heterozygous rs55705857-A/G RIP tumor cells by 4C-seq, which revealed reciprocal physical interactions between the *Myc* TSS and the orthologous rs55705857 element. The heat map color-scale shows normalized median contact frequency. The black trendline shows the median contact frequency.

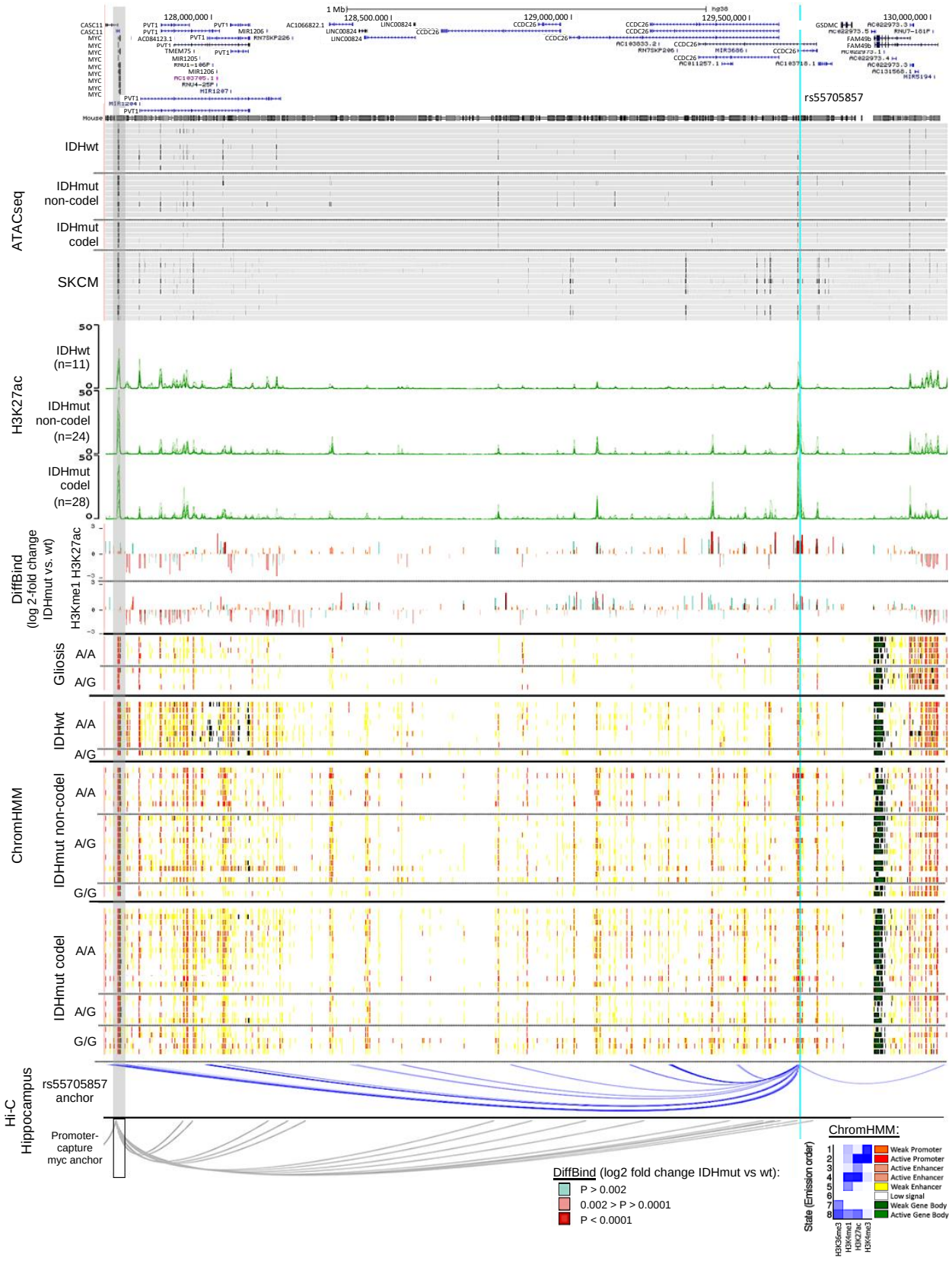

Fig. S19. rs55705857 interacts with MYC promoter and modulates epigenetic landscape of 8q24
Myc-FAM49b (Chr8:127,700,000-130,045,000; hg38) ATAC-seq data for the *IDH*-WT (8 GBM and 1 LGG) and *IDH*-mutant (12 LGG and 1 GBM) brain tumors and skin cutaneous melanoma (SKCM) are

aligned with H3K27ac as well as DiffBind log2-fold change for H3K27ac and H3K4me^{1} when comparing *IDH*-mutant vs *IDH*-WT brain tumors. ChIPseq signals for H3K27ac (dark green) are shown for the Mayo cohort of cases, stratified into *IDH*-WT, *IDH*-mutant non-codel and *IDH*-mutant codel groups. DiffBind shows the fold change and p-value between the *IDH*-mutant vs. *IDH*-WT for both H3K27c and H3K4me^{1}. ChromHMM shows the predicted function of the genome surrounding rs55705857 based on the histone marks H3K36me^{3}, H3K4me^{1}, H3K27ac and H3K4me^{3} in *IDH*-WT and *IDH*-mutant brain tumors as well as non-tumorous gliosis samples. Interactions from Hi-C using the rs55705857 as the anchor point in hippocampus (*33*) and Promoter-capture Hi-C interactions centered at the *MYC* promoter (*32*) are shown. The light blue line marks the location of rs55705857, and shaded gray box marks the location of *MYC*. *IDH*-mutant brain tumors and gliosis samples are sorted by rs55705857 non-risk (A) and risk (G) alleles.

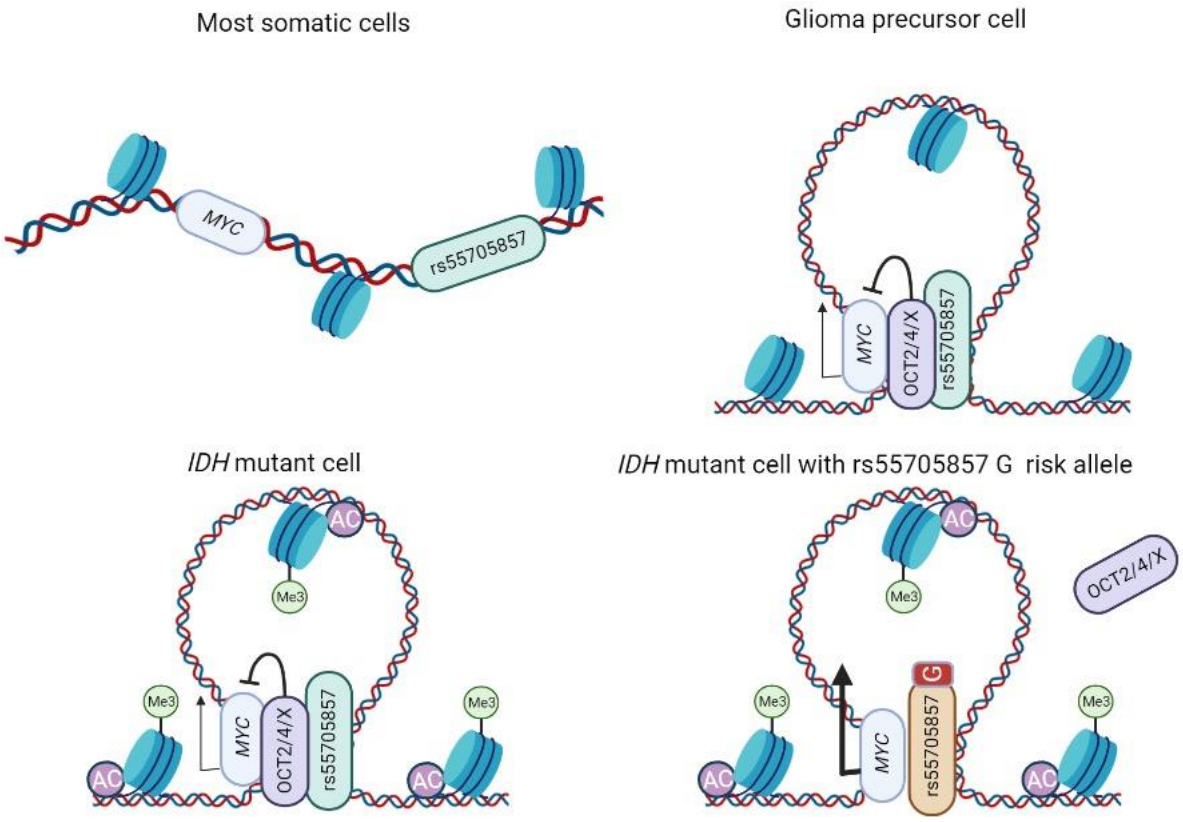

Fig. S20. Schematic describing proposed mechanism of action how rs55705857 regulates MYC
In most somatic cells, *MYC* and rs55705857 are separated through chromosomal topology and do not interact (top left). Within glioma precursor cells, rs55705857 interacts with the *MYC* locus and rs55705857-A allele is bound by OCT transcription factors such as OCT2 or OCT4, which repress *MYC* expression (top right). *IDH1* mutation rewires the epigenetic landscape and chromatin state surrounding the rs55705857 enhancer region leading to an open and hyperactive chromatin state (bottom left). The rs55705857-G risk allele disrupts binding of OCT transcription factors and thus transcriptional repression of *MYC* promoter leading to increased *MYC* expression (bottom right).

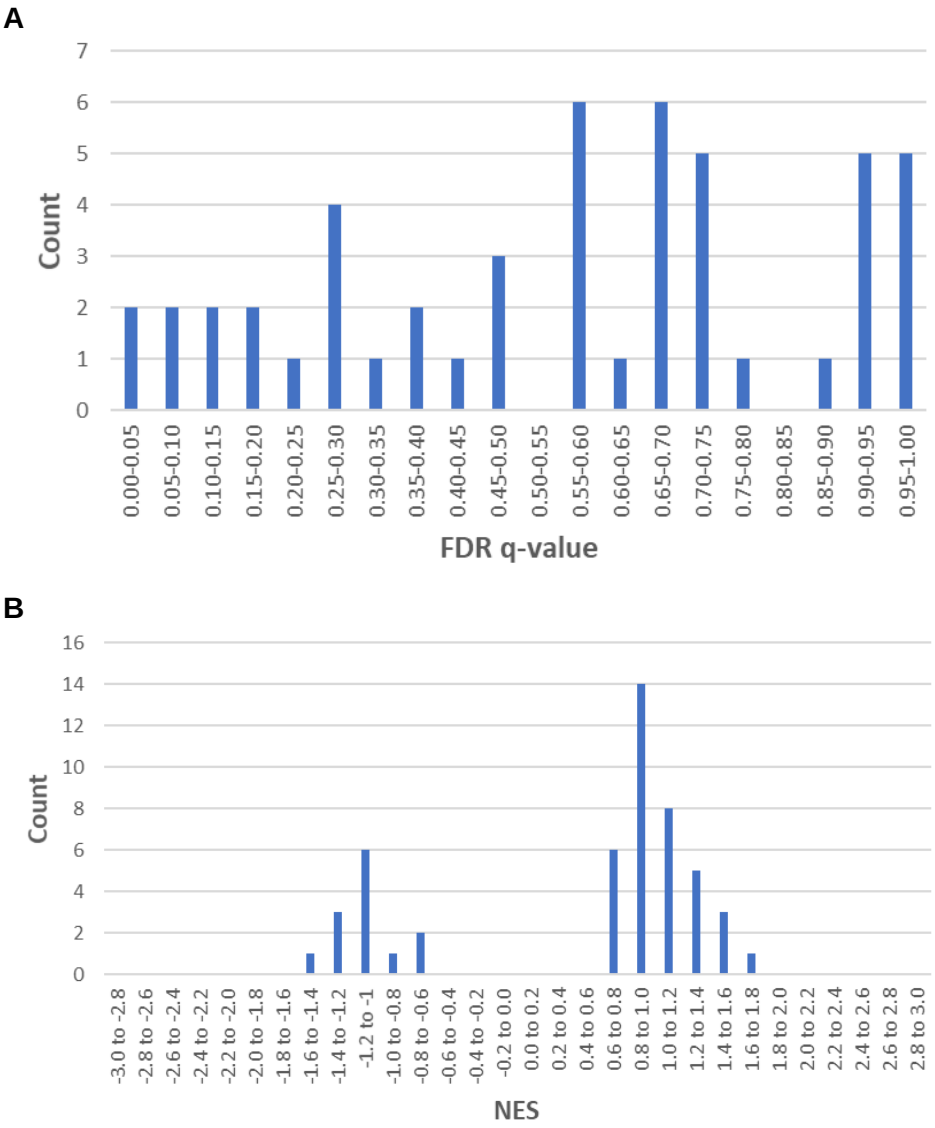

Fig. S21. Control gene sets. (**A** and **B)** Distribution of FDR (A) and NES (B) in 50 randomly selected gene lists**.**

References and Notes

1. A. Sud, B. Kinnersley, R. S. Houlston, Genome-wide association studies of cancer: Current insights and future perspectives. *Nat. Rev. Cancer* **17**, 692–704 (2017). doi:10.1038/nrc.2017.82 Medline

2. D. J. Schaid, W. Chen, N. B. Larson, From genome-wide associations to candidate causal variants by statistical fine-mapping. *Nat. Rev. Genet.* **19**, 491–504 (2018). doi:10.1038/s41576-018-0016-z Medline

3. R. B. Jenkins, M. R. Wrensch, D. Johnson, B. L. Fridley, P. A. Decker, Y. Xiao, T. M. Kollmeyer, A. L. Rynearson, S. Fink, T. Rice, L. S. McCoy, C. Halder, M. L. Kosel, C. Giannini, T. Tihan, B. P. O'Neill, D. H. Lachance, P. Yang, J. Wiemels, J. K. Wiencke, Distinct germ line polymorphisms underlie glioma morphologic heterogeneity. *Cancer Genet.* **204**, 13–18 (2011). doi:10.1016/j.cancergencyto.2010.10.002 Medline

4. R. B. Jenkins, Y. Xiao, H. Sicotte, P. A. Decker, T. M. Kollmeyer, H. M. Hansen, M. L. Kosel, S. Zheng, K. M. Walsh, T. Rice, P. Bracci, L. S. McCoy, I. Smirnov, J. S. Patoka, G. Hsuang, J. L. Wiemels, T. Tihan, A. R. Pico, M. D. Prados, S. M. Chang, M. S. Berger, A. A. Caron, S. R. Fink, C. Halder, A. L. Rynearson, B. L. Fridley, J. C. Buckner, B. P. O'Neill, C. Giannini, D. H. Lachance, J. K. Wiencke, J. E. Eckel-Passow, M. R. Wrensch, A low-frequency variant at 8q24.21 is strongly associated with risk of oligodendroglial tumors and astrocytomas with *IDH1* or *IDH2* mutation. *Nat. Genet.* **44**, 1122–1125 (2012). doi:10.1038/ng.2388 Medline

5. J. E. Eckel-Passow, D. H. Lachance, A. M. Molinaro, K. M. Walsh, P. A. Decker, H. Sicotte, M. Pekmezci, T. Rice, M. L. Kosel, I. V. Smirnov, G. Sarkar, A. A. Caron, T. M. Kollmeyer, C. E. Praska, A. R. Chada, C. Halder, H. M. Hansen, L. S. McCoy, P. M. Bracci, R. Marshall, S. Zheng, G. F. Reis, A. R. Pico, B. P. O'Neill, J. C. Buckner, C. Giannini, J. T. Huse, A. Perry, T. Tihan, M. S. Berger, S. M. Chang, M. D. Prados, J. Wiemels, J. K. Wiencke, M. R. Wrensch, R. B. Jenkins, Glioma groups based on 1p/19q, IDH, and TERT promoter mutations in tumors. *N. Engl. J. Med.* **372**, 2499–2508 (2015). doi:10.1056/NEJMoa1407279 Medline

6. B. S. Melin, J. S. Barnholtz-Sloan, M. R. Wrensch, C. Johansen, D. Il'yasova, B. Kinnersley, Q. T. Ostrom, K. Labreche, Y. Chen, G. Armstrong, Y. Liu, J. E. Eckel-Passow, P. A. Decker, M. Labussière, A. Idbaih, K. Hoang-Xuan, A.-L. Di Stefano, K. Mokhtari, J.-Y. Delattre, P. Broderick, P. Galan, K. Gousias, J. Schramm, M. J. Schoemaker, S. J. Fleming, S. Herms, S. Heilmann, M. M. Nöthen, H.-E. Wichmann, S. Schreiber, A. Swerdlow, M. Lathrop, M. Simon, M. Sanson, U. Andersson, P. Rajaraman, S. Chanock, M. Linet, Z. Wang, M. Yeager, J. K. Wiencke, H. Hansen, L. McCoy, T. Rice, M. L. Kosel, H. Sicotte, C. I. Amos, J. L. Bernstein, F. Davis, D. Lachance, C. Lau, R. T. Merrell, J. Shildkraut, F. Ali-Osman, S. Sadetzki, M. Scheurer, S. Shete, R. K. Lai, E. B. Claus, S. H. Olson, R. B. Jenkins, R. S. Houlston, M. L. Bondy; GliomaScan Consortium, Genome-wide association study of glioma subtypes identifies specific differences in genetic susceptibility to glioblastoma and non-glioblastoma tumors. *Nat. Genet.* **49**, 789–794 (2017). doi:10.1038/ng.3823 Medline

7. J. E. Eckel-Passow, K. L. Drucker, T. M. Kollmeyer, M. L. Kosel, P. A. Decker, A. M. Molinaro, T. Rice, C. E. Praska, L. Clark, A. Caron, A. Abyzov, A. Batzler, J. S. Song, M. Pekmezci, H. M. Hansen, L. S. McCoy, P. M. Bracci, J. Wiemels, J. K. Wiencke, S.

Francis, T. C. Burns, C. Giannini, D. H. Lachance, M. Wrensch, R. B. Jenkins, Adult diffuse glioma GWAS by molecular subtype identifies variants in *D2HGDH* and *FAM20C*. *Neuro-Oncology* **22**, 1602–1613 (2020). doi:10.1093/neuonc/noaa117 Medline

8. Y. Oktay, E. Ülgen, Ö. Can, C. B. Akyerli, Ş. Yüksel, Y. Erdemgil, İ. M. Durası, O. I. Henegariu, E. P. Nanni, N. Selevsek, J. Grossmann, E. Z. Erson-Omay, H. Bai, M. Gupta, W. Lee, Ş. Turcan, A. Özpınar, J. T. Huse, M. A. Sav, A. Flanagan, M. Günel, O. U. Sezerman, M. C. Yakıcıer, M. N. Pamir, K. Özduman, IDH-mutant glioma specific association of rs55705857 located at 8q24.21 involves MYC deregulation. *Sci. Rep.* **6**, 27569 (2016). doi:10.1038/srep27569 Medline

9. L. Dang, D. W. White, S. Gross, B. D. Bennett, M. A. Bittinger, E. M. Driggers, V. R. Fantin, H. G. Jang, S. Jin, M. C. Keenan, K. M. Marks, R. M. Prins, P. S. Ward, K. E. Yen, L. M. Liau, J. D. Rabinowitz, L. C. Cantley, C. B. Thompson, M. G. Vander Heiden, S. M. Su, Cancer-associated IDH1 mutations produce 2-hydroxyglutarate. *Nature* **462**, 739–744 (2009). doi:10.1038/nature08617 Medline

10. F. Fack, S. Tardito, G. Hochart, A. Oudin, L. Zheng, S. Fritah, A. Golebiewska, P. V. Nazarov, A. Bernard, A.-C. Hau, O. Keunen, W. Leenders, M. Lund-Johansen, J. Stauber, E. Gottlieb, R. Bjerkvig, S. P. Niclou, Altered metabolic landscape in IDH-mutant gliomas affects phospholipid, energy, and oxidative stress pathways. *EMBO Mol. Med.* **9**, 1681–1695 (2017). doi:10.15252/emmm.201707729 Medline

11. C. Lu, P. S. Ward, G. S. Kapoor, D. Rohle, S. Turcan, O. Abdel-Wahab, C. R. Edwards, R. Khanin, M. E. Figueroa, A. Melnick, K. E. Wellen, D. M. O'Rourke, S. L. Berger, T. A. Chan, R. L. Levine, I. K. Mellinghoff, C. B. Thompson, IDH mutation impairs histone demethylation and results in a block to cell differentiation. *Nature* **483**, 474–478 (2012). doi:10.1038/nature10860 Medline

12. R. A. Cairns, T. W. Mak, Oncogenic isocitrate dehydrogenase mutations: Mechanisms, models, and clinical opportunities. *Cancer Discov.* **3**, 730–741 (2013). doi:10.1158/2159-8290.CD-13-0083 Medline

13. S. Chang, S. Yim, H. Park, The cancer driver genes *IDH1/2*, *JARID1C/KDM5C*, and *UTX/KDM6A*: Crosstalk between histone demethylation and hypoxic reprogramming in cancer metabolism. *Exp. Mol. Med.* **51**, 1–17 (2019). doi:10.1038/s12276-019-0230-6 Medline

14. H. Suzuki, K. Aoki, K. Chiba, Y. Sato, Y. Shiozawa, Y. Shiraishi, T. Shimamura, A. Niida, K. Motomura, F. Ohka, T. Yamamoto, K. Tanahashi, M. Ranjit, T. Wakabayashi, T. Yoshizato, K. Kataoka, K. Yoshida, Y. Nagata, A. Sato-Otsubo, H. Tanaka, M. Sanada, Y. Kondo, H. Nakamura, M. Mizoguchi, T. Abe, Y. Muragaki, R. Watanabe, I. Ito, S. Miyano, A. Natsume, S. Ogawa, Mutational landscape and clonal architecture in grade II and III gliomas. *Nat. Genet.* **47**, 458–468 (2015). doi:10.1038/ng.3273 Medline

15. D. N. Louis, A. Perry, G. Reifenberger, A. von Deimling, D. Figarella-Branger, W. K. Cavenee, H. Ohgaki, O. D. Wiestler, P. Kleihues, D. W. Ellison, The 2016 World Health Organization Classification of Tumors of the Central Nervous System: A summary. *Acta Neuropathol.* **131**, 803–820 (2016). doi:10.1007/s00401-016-1545-1 Medline

16. M. R. Corces, J. M. Granja, S. Shams, B. H. Louie, J. A. Seoane, W. Zhou, T. C. Silva, C. Groeneveld, C. K. Wong, S. W. Cho, A. T. Satpathy, M. R. Mumbach, K. A. Hoadley, A. G. Robertson, N. C. Sheffield, I. Felau, M. A. A. Castro, B. P. Berman, L. M. Staudt, J.

C. Zenklusen, P. W. Laird, C. Curtis, W. J. Greenleaf, H. Y. Chang; Cancer Genome Atlas Analysis Network, The chromatin accessibility landscape of primary human cancers. *Science* **362**, eaav1898 (2018). doi:10.1126/science.aav1898 Medline

17. O. Lancho, D. Herranz, The MYC enhancer-ome: long-range transcriptional regulation of MYC in cancer. *Trends Cancer* **4**, 810–822 (2018). doi:10.1016/j.trecan.2018.10.003 Medline

18. E. Z. Kvon, Y. Zhu, G. Kelman, C. S. Novak, I. Plajzer-Frick, M. Kato, T. H. Garvin, Q. Pham, A. N. Harrington, R. D. Hunter, J. Godoy, E. M. Meky, J. A. Akiyama, V. Afzal, S. Tran, F. Escande, B. Gilbert-Dussardier, N. Jean-Marçais, S. Hudaiberdiev, I. Ovcharenko, M. B. Dobbs, C. A. Gurnett, S. Manouvrier-Hanu, F. Petit, A. Visel, D. E. Dickel, L. A. Pennacchio, Comprehensive in vivo interrogation reveals phenotypic impact of human enhancer variants. *Cell* **180**, 1262–1271.e15 (2020). doi:10.1016/j.cell.2020.02.031 Medline

19. M. Sasaki, C. B. Knobbe, J. C. Munger, E. F. Lind, D. Brenner, A. Brüstle, I. S. Harris, R. Holmes, A. Wakeham, J. Haight, A. You-Ten, W. Y. Li, S. Schalm, S. M. Su, C. Virtanen, G. Reifenberger, P. S. Ohashi, D. L. Barber, M. E. Figueroa, A. Melnick, J.-C. Zúñiga-Pflücker, T. W. Mak, IDH1(R132H) mutation increases murine haematopoietic progenitors and alters epigenetics. *Nature* **488**, 656–659 (2012). doi:10.1038/nature11323 Medline

20. Y. Stein, R. Aloni-Grinstein, V. Rotter, Mutant p53 oncogenicity: Dominant-negative or gain-of-function? *Carcinogenesis* **41**, 1635–1647 (2020). doi:10.1093/carcin/bgaa117 Medline

21. T. Jacks, L. Remington, B. O. Williams, E. M. Schmitt, S. Halachmi, R. T. Bronson, R. A. Weinberg, Tumor spectrum analysis in *p53*-mutant mice. *Curr. Biol.* **4**, 1–7 (1994). doi:10.1016/S0960-9822(00)00002-6 Medline

22. K. P. Olive, D. A. Tuveson, Z. C. Ruhe, B. Yin, N. A. Willis, R. T. Bronson, D. Crowley, T. Jacks, Mutant *p53* gain of function in two mouse models of Li-Fraumeni syndrome. *Cell* **119**, 847–860 (2004). doi:10.1016/j.cell.2004.11.004 Medline

23. C. Bardella, O. Al-Dalahmah, D. Krell, P. Brazauskas, K. Al-Qahtani, M. Tomkova, J. Adam, S. Serres, H. Lockstone, L. Freeman-Mills, I. Pfeffer, N. Sibson, R. Goldin, B. Schuster-Böeckler, P. J. Pollard, T. Soga, J. S. McCullagh, C. J. Schofield, P. Mulholland, O. Ansorge, S. Kriaucionis, P. J. Ratcliffe, F. G. Szele, I. Tomlinson, Expression of $Idh1^{R132H}$ in the murine subventricular zone stem cell niche recapitulates features of early gliomagenesis. *Cancer Cell* **30**, 578–594 (2016). doi:10.1016/j.ccell.2016.08.017 Medline

24. C. J. Pirozzi, A. B. Carpenter, M. S. Waitkus, C. Y. Wang, H. Zhu, L. J. Hansen, L. H. Chen, P. K. Greer, J. Feng, Y. Wang, C. B. Bock, P. Fan, I. Spasojevic, R. E. McLendon, D. D. Bigner, Y. He, H. Yan, Mutant IDH1 disrupts the mouse subventricular zone and alters brain tumor progression. *Mol. Cancer Res.* **15**, 507–520 (2017). doi:10.1158/1541-7786.MCR-16-0485 Medline

25. J. Hsieh, Orchestrating transcriptional control of adult neurogenesis. *Genes Dev.* **26**, 1010–1021 (2012). doi:10.1101/gad.187336.112 Medline

26. A. L. Ferri, M. Cavallaro, D. Braida, A. Di Cristofano, A. Canta, A. Vezzani, S. Ottolenghi, P. P. Pandolfi, M. Sala, S. DeBiasi, S. K. Nicolis, *Sox2* deficiency causes neurodegeneration and impaired neurogenesis in the adult mouse brain. *Development* **131**, 3805–3819 (2004). doi:10.1242/dev.01204 Medline

27. H. Suh, A. Consiglio, J. Ray, T. Sawai, K. A. D'Amour, F. H. Gage, In vivo fate analysis reveals the multipotent and self-renewal capacities of *Sox2*$^+$ neural stem cells in the adult hippocampus. *Cell Stem Cell* **1**, 515–528 (2007). doi:10.1016/j.stem.2007.09.002 Medline

28. R. L. Reeve, S. Z. Yammine, C. M. Morshead, D. van der Kooy, Quiescent Oct4$^+$ neural stem cells (NSCs) repopulate ablated glial fibrillary acidic protein$^+$ NSCs in the adult mouse brain. *Stem Cells* **35**, 2071–2082 (2017). doi:10.1002/stem.2662 Medline

29. N. I. Park, P. Guilhamon, K. Desai, R. F. McAdam, E. Langille, M. O'Connor, X. Lan, H. Whetstone, F. J. Coutinho, R. J. Vanner, E. Ling, P. Prinos, L. Lee, H. Selvadurai, G. Atwal, M. Kushida, I. D. Clarke, V. Voisin, M. D. Cusimano, M. Bernstein, S. Das, G. Bader, C. H. Arrowsmith, S. Angers, X. Huang, M. Lupien, P. B. Dirks, ASCL1 reorganizes chromatin to direct neuronal fate and suppress tumorigenicity of glioblastoma stem cells. *Cell Stem Cell* **21**, 411 (2017). doi:10.1016/j.stem.2017.08.008 Medline

30. H. Bulstrode, E. Johnstone, M. A. Marques-Torrejon, K. M. Ferguson, R. B. Bressan, C. Blin, V. Grant, S. Gogolok, E. Gangoso, S. Gagrica, C. Ender, V. Fotaki, D. Sproul, P. Bertone, S. M. Pollard, Elevated FOXG1 and SOX2 in glioblastoma enforces neural stem cell identity through transcriptional control of cell cycle and epigenetic regulators. *Genes Dev.* **31**, 757–773 (2017). doi:10.1101/gad.293027.116 Medline

31. H. Ikushima, T. Todo, Y. Ino, M. Takahashi, N. Saito, K. Miyazawa, K. Miyazono, Glioma-initiating cells retain their tumorigenicity through integration of the Sox axis and Oct4 protein. *J. Biol. Chem.* **286**, 41434–41441 (2011). doi:10.1074/jbc.M111.300863 Medline

32. W. Winick-Ng, A. Kukalev, I. Harabula, L. Zea-Redondo, D. Szabó, M. Meijer, L. Serebreni, Y. Zhang, S. Bianco, A. M. Chiariello, I. Irastorza-Azcarate, C. J. Thieme, T. M. Sparks, S. Carvalho, L. Fiorillo, F. Musella, E. Irani, E. Torlai Triglia, A. A. Kolodziejczyk, A. Abentung, G. Apostolova, E. J. Paul, V. Franke, R. Kempfer, A. Akalin, S. A. Teichmann, G. Dechant, M. A. Ungless, M. Nicodemi, L. Welch, G. Castelo-Branco, A. Pombo, Cell-type specialization is encoded by specific chromatin topologies. *Nature* **599**, 684–691 (2021). doi:10.1038/s41586-021-04081-2 Medline

33. D. Yang, I. Jang, J. Choi, M.-S. Kim, A. J. Lee, H. Kim, J. Eom, D. Kim, I. Jung, B. Lee, 3DIV: A 3D-genome Interaction Viewer and database. *Nucleic Acids Res.* **46**, D52–D57 (2018). doi:10.1093/nar/gkx1017 Medline

34. I. Jung, A. Schmitt, Y. Diao, A. J. Lee, T. Liu, D. Yang, C. Tan, J. Eom, M. Chan, S. Chee, Z. Chiang, C. Kim, E. Masliah, C. L. Barr, B. Li, S. Kuan, D. Kim, B. Ren, A compendium of promoter-centered long-range chromatin interactions in the human genome. *Nat. Genet.* **51**, 1442–1449 (2019). doi:10.1038/s41588-019-0494-8 Medline

35. P. M. Scarbrough, I. Akushevich, M. Wrensch, D. Il'yasova, Exploring the association between melanoma and glioma risks. *Ann. Epidemiol.* **24**, 469–474 (2014). doi:10.1016/j.annepidem.2014.02.010 Medline

36. A. K. Chan, S. J. Han, W. Choy, D. Beleford, M. K. Aghi, M. S. Berger, J. T. Shieh, A. W. Bollen, A. Perry, J. J. Phillips, N. Butowski, D. A. Solomon, Familial melanoma-astrocytoma syndrome: Synchronous diffuse astrocytoma and pleomorphic xanthoastrocytoma in a patient with germline CDKN2A/B deletion and a significant family history. *Clin. Neuropathol.* **36**, 213–221 (2017). doi:10.5414/NP301022 Medline

37. P. J. Killela, Z. J. Reitman, Y. Jiao, C. Bettegowda, N. Agrawal, L. A. Diaz Jr., A. H. Friedman, H. Friedman, G. L. Gallia, B. C. Giovanella, A. P. Grollman, T.-C. He, Y. He, R. H. Hruban, G. I. Jallo, N. Mandahl, A. K. Meeker, F. Mertens, G. J. Netto, B. A. Rasheed, G. J. Riggins, T. A. Rosenquist, M. Schiffman, IeM. Shih, D. Theodorescu, M. S. Torbenson, V. E. Velculescu, T.-L. Wang, N. Wentzensen, L. D. Wood, M. Zhang, R. E. McLendon, D. D. Bigner, K. W. Kinzler, B. Vogelstein, N. Papadopoulos, H. Yan, *TERT* promoter mutations occur frequently in gliomas and a subset of tumors derived from cells with low rates of self-renewal. *Proc. Natl. Acad. Sci. U.S.A.* **110**, 6021–6026 (2013). doi:10.1073/pnas.1303607110 Medline

38. M. N. Bainbridge, G. N. Armstrong, M. M. Gramatges, A. A. Bertuch, S. N. Jhangiani, H. Doddapaneni, L. Lewis, J. Tombrello, S. Tsavachidis, Y. Liu, A. Jalali, S. E. Plon, C. C. Lau, D. W. Parsons, E. B. Claus, J. Barnholtz-Sloan, D. Il'yasova, J. Schildkraut, F. Ali-Osman, S. Sadetzki, C. Johansen, R. S. Houlston, R. B. Jenkins, D. Lachance, S. H. Olson, J. L. Bernstein, R. T. Merrell, M. R. Wrensch, K. M. Walsh, F. G. Davis, R. Lai, S. Shete, K. Aldape, C. I. Amos, P. A. Thompson, D. M. Muzny, R. A. Gibbs, B. S. Melin, M. L. Bondy; Gliogene Consortium, Germline mutations in shelterin complex genes are associated with familial glioma. *J. Natl. Cancer Inst.* **107**, 384 (2014). doi:10.1093/jnci/dju384 Medline

39. H. Niwa, Y. Toyooka, D. Shimosato, D. Strumpf, K. Takahashi, R. Yagi, J. Rossant, Interaction between Oct3/4 and Cdx2 determines trophectoderm differentiation. *Cell* **123**, 917–929 (2005). doi:10.1016/j.cell.2005.08.040 Medline

40. G. J. Pan, Z. Y. Chang, H. R. Schöler, D. Pei, Stem cell pluripotency and transcription factor Oct4. *Cell Res.* **12**, 321–329 (2002). doi:10.1038/sj.cr.7290134 Medline

41. E. Theodorou, G. Dalembert, C. Heffelfinger, E. White, S. Weissman, L. Corcoran, M. Snyder, A high throughput embryonic stem cell screen identifies Oct-2 as a bifunctional regulator of neuronal differentiation. *Genes Dev.* **23**, 575–588 (2009). doi:10.1101/gad.1772509 Medline

42. S. Ryall, U. Tabori, C. Hawkins, Pediatric low-grade glioma in the era of molecular diagnostics. *Acta Neuropathol. Commun.* **8**, 30 (2020). doi:10.1186/s40478-020-00902-z Medline

43. M. Sasaki, C. B. Knobbe, M. Itsumi, A. J. Elia, I. S. Harris, I. I. C. Chio, R. A. Cairns, S. McCracken, A. Wakeham, J. Haight, A. Y. Ten, B. Snow, T. Ueda, S. Inoue, K. Yamamoto, M. Ko, A. Rao, K. E. Yen, S. M. Su, T. W. Mak, D-2-hydroxyglutarate produced by mutant IDH1 perturbs collagen maturation and basement membrane function. *Genes Dev.* **26**, 2038–2049 (2012). doi:10.1101/gad.198200.112 Medline

44. J. Ganz, E. A. Maury, B. Becerra, S. Bizzotto, R. N. Doan, C. J. Kenny, T. Shin, J. Kim, Z. Zhou, K. L. Ligon, E. A. Lee, C. A. Walsh, Rates and patterns of clonal oncogenic mutations in the normal human brain. *Cancer Discov.* **12**, 172–185 (2022). doi:10.1158/2159-8290.CD-21-0245 Medline

45. K. Labreche, B. Kinnersley, G. Berzero, A. L. Di Stefano, A. Rahimian, I. Detrait, Y. Marie, B. Grenier-Boley, K. Hoang-Xuan, J.-Y. Delattre, A. Idbaih, R. S. Houlston, M. Sanson, Diffuse gliomas classified by 1p/19q co-deletion, *TERT* promoter and IDH mutation status are associated with specific genetic risk loci. *Acta Neuropathol.* **135**, 743–755 (2018). doi:10.1007/s00401-018-1825-z Medline

46. M. Wrensch, R. B. Jenkins, J. S. Chang, R.-F. Yeh, Y. Xiao, P. A. Decker, K. V. Ballman, M. Berger, J. C. Buckner, S. Chang, C. Giannini, C. Halder, T. M. Kollmeyer, M. L. Kosel, D. H. LaChance, L. McCoy, B. P. O'Neill, J. Patoka, A. R. Pico, M. Prados, C. Quesenberry, T. Rice, A. L. Rynearson, I. Smirnov, T. Tihan, J. Wiemels, P. Yang, J. K. Wiencke, Variants in the *CDKN2B* and *RTEL1* regions are associated with high-grade glioma susceptibility. *Nat. Genet.* **41**, 905–908 (2009). doi:10.1038/ng.408 Medline

47. V. Enciso-Mora, F. J. Hosking, B. Kinnersley, Y. Wang, S. Shete, D. Zelenika, P. Broderick, A. Idbaih, J.-Y. Delattre, K. Hoang-Xuan, Y. Marie, A. L. Di Stefano, M. Labussière, S. Dobbins, B. Boisselier, P. Ciccarino, M. Rossetto, G. Armstrong, Y. Liu, K. Gousias, J. Schramm, C. Lau, S. J. Hepworth, K. Strauch, M. Müller-Nurasyid, S. Schreiber, A. Franke, S. Moebus, L. Eisele, A. Forsti, K. Hemminki, I. P. Tomlinson, A. Swerdlow, M. Lathrop, M. Simon, M. Bondy, M. Sanson, R. S. Houlston, Deciphering the 8q24.21 association for glioma. *Hum. Mol. Genet.* **22**, 2293–2302 (2013). doi:10.1093/hmg/ddt063 Medline

48. J. Zhong, Z. Ye, S. W. Lenz, C. R. Clark, A. Bharucha, G. Farrugia, K. D. Robertson, Z. Zhang, T. Ordog, J.-H. Lee, Purification of nanogram-range immunoprecipitated DNA in ChIP-seq application. *BMC Genomics* **18**, 985 (2017). doi:10.1186/s12864-017-4371-5 Medline

49. K. R. Kalari, A. A. Nair, J. D. Bhavsar, D. R. O'Brien, J. I. Davila, M. A. Bockol, J. Nie, X. Tang, S. Baheti, J. B. Doughty, S. Middha, H. Sicotte, A. E. Thompson, Y. W. Asmann, J.-P. A. Kocher, MAP-RSeq: Mayo Analysis Pipeline for RNA sequencing. *BMC Bioinformatics* **15**, 224 (2014). doi:10.1186/1471-2105-15-224 Medline

50. A. Dobin, C. A. Davis, F. Schlesinger, J. Drenkow, C. Zaleski, S. Jha, P. Batut, M. Chaisson, T. R. Gingeras, STAR: Ultrafast universal RNA-seq aligner. *Bioinformatics* **29**, 15–21 (2013). doi:10.1093/bioinformatics/bts635 Medline

51. Y. Liao, G. K. Smyth, W. Shi, The Subread aligner: Fast, accurate and scalable read mapping by seed-and-vote. *Nucleic Acids Res.* **41**, e108 (2013). doi:10.1093/nar/gkt214 Medline

52. L. Wang, S. Wang, W. Li, RSeQC: Quality control of RNA-seq experiments. *Bioinformatics* **28**, 2184–2185 (2012). doi:10.1093/bioinformatics/bts356 Medline

53. M. D. Robinson, D. J. McCarthy, G. K. Smyth, edgeR: A Bioconductor package for differential expression analysis of digital gene expression data. *Bioinformatics* **26**, 139–140 (2010). doi:10.1093/bioinformatics/btp616 Medline

54. D. J. McCarthy, Y. Chen, G. K. Smyth, Differential expression analysis of multifactor RNA-Seq experiments with respect to biological variation. *Nucleic Acids Res.* **40**, 4288–4297 (2012). doi:10.1093/nar/gks042 Medline

55. S. Zhao, L. Yin, Y. Guo, Q. Sheng, Y. Shyr, heatmap3: An Improved Heatmap Package, R package version 1.1.7 (2020); https://CRAN.R-project.org/package=heatmap3.

56. L. Collado-Torres, A. Nellore, K. Kammers, S. E. Ellis, M. A. Taub, K. D. Hansen, A. E. Jaffe, B. Langmead, J. T. Leek, Reproducible RNA-seq analysis using recount2. *Nat. Biotechnol.* **35**, 319–321 (2017). doi:10.1038/nbt.3838 Medline

57. M. Ceccarelli, F. P. Barthel, T. M. Malta, T. S. Sabedot, S. R. Salama, B. A. Murray, O. Morozova, Y. Newton, A. Radenbaugh, S. M. Pagnotta, S. Anjum, J. Wang, G. Manyam, P. Zoppoli, S. Ling, A. A. Rao, M. Grifford, A. D. Cherniack, H. Zhang, L. Poisson, C. G. Carlotti Jr., D. P. C. Tirapelli, A. Rao, T. Mikkelsen, C. C. Lau, W. K. A. Yung, R. Rabadan, J. Huse, D. J. Brat, N. L. Lehman, J. S. Barnholtz-Sloan, S. Zheng, K. Hess, G. Rao, M. Meyerson, R. Beroukhim, L. Cooper, R. Akbani, M. Wrensch, D. Haussler, K. D. Aldape, P. W. Laird, D. H. Gutmann, H. Noushmehr, A. Iavarone, R. G. W. Verhaak; TCGA Research Network, Molecular profiling reveals biologically discrete subsets and pathways of progression in diffuse glioma. *Cell* **164**, 550–563 (2016). doi:10.1016/j.cell.2015.12.028 Medline

58. R. Stark, G. Brown, DiffBind: differential binding analysis of ChIP-seq peak data (2011); http://bioconductor.org/packages/release/bioc/html/DiffBind.html.

59. M. I. Love, W. Huber, S. Anders, Moderated estimation of fold change and dispersion for RNA-seq data with DESeq2. *Genome Biol.* **15**, 550 (2014). doi:10.1186/s13059-014-0550-8 Medline

60. H. Yan, J. Evans, M. Kalmbach, R. Moore, S. Middha, S. Luban, L. Wang, A. Bhagwate, Y. Li, Z. Sun, X. Chen, J.-P. A. Kocher, HiChIP: A high-throughput pipeline for integrative analysis of ChIP-Seq data. *BMC Bioinformatics* **15**, 280 (2014). doi:10.1186/1471-2105-15-280 Medline

61. H. Li, B. Handsaker, A. Wysoker, T. Fennell, J. Ruan, N. Homer, G. Marth, G. Abecasis, R. Durbin; 1000 Genome Project Data Processing Subgroup, The Sequence Alignment/Map format and SAMtools. *Bioinformatics* **25**, 2078–2079 (2009). doi:10.1093/bioinformatics/btp352 Medline

62. Y. Zhang, T. Liu, C. A. Meyer, J. Eeckhoute, D. S. Johnson, B. E. Bernstein, C. Nusbaum, R. M. Myers, M. Brown, W. Li, X. S. Liu, Model-based Analysis of ChIP-Seq (MACS). *Genome Biol.* **9**, R137 (2008). doi:10.1186/gb-2008-9-9-r137 Medline

63. S. Xu, S. Grullon, K. Ge, W. Peng, Spatial clustering for identification of ChIP-enriched regions (SICER) to map regions of histone methylation patterns in embryonic stem cells. *Methods Mol. Biol.* **1150**, 97–111 (2014). doi:10.1007/978-1-4939-0512-6_5 Medline

64. X. Ji, W. Li, J. Song, L. Wei, X. S. Liu, CEAS: *cis*-regulatory element annotation system. *Nucleic Acids Res.* **34** (suppl. 2), W551–W554 (2006). doi:10.1093/nar/gkl322 Medline

65. C. Y. McLean, D. Bristor, M. Hiller, S. L. Clarke, B. T. Schaar, C. B. Lowe, A. M. Wenger, G. Bejerano, GREAT improves functional interpretation of *cis*-regulatory regions. *Nat. Biotechnol.* **28**, 495–501 (2010). doi:10.1038/nbt.1630 Medline

66. F. Ramírez, D. P. Ryan, B. Grüning, V. Bhardwaj, F. Kilpert, A. S. Richter, S. Heyne, F. Dündar, T. Manke, deepTools2: A next generation web server for deep-sequencing data analysis. *Nucleic Acids Res.* **44**, W160–W165 (2016). doi:10.1093/nar/gkw257 Medline

67. J. Ernst, M. Kellis, ChromHMM: Automating chromatin-state discovery and characterization. *Nat. Methods* **9**, 215–216 (2012). doi:10.1038/nmeth.1906 Medline

68. S. Heinz, C. Benner, N. Spann, E. Bertolino, Y. C. Lin, P. Laslo, J. X. Cheng, C. Murre, H. Singh, C. K. Glass, Simple combinations of lineage-determining transcription factors prime *cis*-regulatory elements required for macrophage and B cell identities. *Mol. Cell* **38**, 576–589 (2010). doi:10.1016/j.molcel.2010.05.004 Medline

69. F. Lemonnier, R. A. Cairns, S. Inoue, W. Y. Li, A. Dupuy, S. Broutin, N. Martin, V. Fataccioli, R. Pelletier, A. Wakeham, B. E. Snow, L. de Leval, A. Pujals, C. Haioun, A. Paci, E. R. Tobin, R. Narayanaswamy, K. Yen, S. Jin, P. Gaulard, T. W. Mak, The IDH2 R172K mutation associated with angioimmunoblastic T-cell lymphoma produces 2HG in T cells and impacts lymphoid development. *Proc. Natl. Acad. Sci. U.S.A.* **113**, 15084–15089 (2016). doi:10.1073/pnas.1617929114 Medline

70. F. Radtke, A. Wilson, G. Stark, M. Bauer, J. van Meerwijk, H. R. MacDonald, M. Aguet, Deficient T cell fate specification in mice with an induced inactivation of *Notch1*. *Immunity* **10**, 547–558 (1999). doi:10.1016/S1074-7613(00)80054-0 Medline

71. P. D. Hsu, D. A. Scott, J. A. Weinstein, F. A. Ran, S. Konermann, V. Agarwala, Y. Li, E. J. Fine, X. Wu, O. Shalem, T. J. Cradick, L. A. Marraffini, G. Bao, F. Zhang, DNA targeting specificity of RNA-guided Cas9 nucleases. *Nat. Biotechnol.* **31**, 827–832 (2013). doi:10.1038/nbt.2647 Medline

72. C. D. Richardson, G. J. Ray, M. A. DeWitt, G. L. Curie, J. E. Corn, Enhancing homology-directed genome editing by catalytically active and inactive CRISPR-Cas9 using asymmetric donor DNA. *Nat. Biotechnol.* **34**, 339–344 (2016). doi:10.1038/nbt.3481 Medline

73. S. K. Loganathan, K. Schleicher, A. Malik, R. Quevedo, E. Langille, K. Teng, R. H. Oh, B. Rathod, R. Tsai, P. Samavarchi-Tehrani, T. J. Pugh, A.-C. Gingras, D. Schramek, Rare driver mutations in head and neck squamous cell carcinomas converge on NOTCH signaling. *Science* **367**, 1264–1269 (2020). doi:10.1126/science.aax0902 Medline

74. S. K. Loganathan, A. Malik, E. Langille, C. Luxenburg, D. Schramek, In vivo CRISPR/Cas9 screening to simultaneously evaluate gene function in mouse skin and oral cavity. *J. Vis. Exp.* **2020**, e61693 (2020). doi:10.3791/61693 Medline

75. B. Mathon, M. Nassar, J. Simonnet, C. Le Duigou, S. Clemenceau, R. Miles, D. Fricker, Increasing the effectiveness of intracerebral injections in adult and neonatal mice: A neurosurgical point of view. *Neurosci. Bull.* **31**, 685–696 (2015). doi:10.1007/s12264-015-1558-0 Medline

76. J. Y. Kim, S. D. Grunke, Y. Levites, T. E. Golde, J. L. Jankowsky, Intracerebroventricular viral injection of the neonatal mouse brain for persistent and widespread neuronal transduction. *J. Vis. Exp.* **2014**, e51863 (2014). doi:10.3791/51863 Medline

77. A. M. Abdel Rahman, J. Pawling, M. Ryczko, A. A. Caudy, J. W. Dennis, Targeted metabolomics in cultured cells and tissues by mass spectrometry: Method development and validation. *Anal. Chim. Acta* **845**, 53–61 (2014). doi:10.1016/j.aca.2014.06.012 Medline

78. J. Chong, D. S. Wishart, J. Xia, Using MetaboAnalyst 4.0 for comprehensive and integrative metabolomics data analysis. *Curr. Protoc. Bioinformatics* **68**, e86 (2019). doi:10.1002/cpbi.86 Medline

79. H. J. van de Werken, G. Landan, S. J. B. Holwerda, M. Hoichman, P. Klous, R. Chachik, E. Splinter, C. Valdes-Quezada, Y. Öz, B. A. M. Bouwman, M. J. A. M. Verstegen, E. de Wit, A. Tanay, W. de Laat, Robust 4C-seq data analysis to screen for regulatory DNA interactions. *Nat. Methods* **9**, 969–972 (2012). doi:10.1038/nmeth.2173 Medline

80. J. Reimand, R. Isserlin, V. Voisin, M. Kucera, C. Tannus-Lopes, A. Rostamianfar, L. Wadi, M. Meyer, J. Wong, C. Xu, D. Merico, G. D. Bader, Pathway enrichment analysis and visualization of omics data using g:Profiler, GSEA, Cytoscape and EnrichmentMap. *Nat. Protoc.* **14**, 482–517 (2019). doi:10.1038/s41596-018-0103-9 Medline

81. A. Menssen, H. Hermeking, Characterization of the c-MYC-regulated transcriptome by SAGE: Identification and analysis of c-MYC target genes. *Proc. Natl. Acad. Sci. U.S.A.* **99**, 6274–6279 (2002). doi:10.1073/pnas.082005599 Medline